Cleaner Chemical Engineering 3 (2022) 100034

Contents lists available at ScienceDirect

Cleaner Chemical Engineering

journal homepage: www.elsevier.com/locate/clce

Photocatalytic, electrochemical, antibacterial and antioxidant behaviour of carbon-sulphur Co-doped zirconium (IV) oxide nanocomposite

J.O. Tijani[a,d,*], E.I. Odeh[a], S. Mustapha[a,d], T.C. Egbosiuba[d,e], A.I. Daniel[c], A.S. Abdulkareem[b,d], F.N. Muya[f]

[a] Department of Chemistry, Federal University of Technology, PMB 65, Minna, Niger, Nigeria
[b] Department of Chemical Engineering, Federal University of Technology, PMB 65, Minna, Niger, Nigeria
[c] Department of Biochemistry, Federal University of Technology, PMB 65, Minna, Niger, Nigeria
[d] Nanotechnology Research Group, African Centre of Excellence on Mycotoxin and Food Safety (ACEMFS), Federal University of Technology, PMB 65, Bosso, Minna, Niger, Nigeria
[e] Department of Chemical Engineering, Chukwuemeka Odumegwu Ojukwu University, PMB 02, Uli Campus, Anambra, Nigeria
[f] Department of Chemistry, SensorLab, University of the Western Cape, PB X17, Bellville 7535, South Africa

ARTICLE INFO

Keywords:
Zirconium oxide
Non-metals doping
Photocatalytic
Electrochemical
Antioxidant
Antibacterial

ABSTRACT

In this work, carbon-sulphur co-doped ZrO_2 nanocomposites were synthesised using the aqueous leaves extract of *Plumeria acuminate,* zirconia salt precursor, polyvinylpyrrolidone and sodium hydrosulphide. The structural, elemental and morphological properties of the synthesized nanomaterials were examined by different analytical techniques UV-visible spectrophotometer, HRSEM-EDS, HRTEM-SAED, XRD and BET. HRSEM analysis of C-S-ZrO_2 revealed the presence of spherical and irregular hexagonal shapes. The XRD pattern demonstrated formation of crystalline tetragonal and a mixture of tetragonal and orthorhombic phases for ZrO_2 and C-S-ZrO_2 composite with an average size of 20.03 nm and 12.40 nm respectively. The band gap values of 5.2 eV and 3.4 eV were obtained for ZrO_2 and C-S-ZrO_2 respectively. The adsorptive and photocatalytic properties of ZrO_2 based nanomaterials for the removal of azo dye in local dyeing wastewater were investigated. The electrochemical activities of the nanomaterials were assessed using cyclic voltammetry, while Agar well diffusion, DPPH and ABTS methods were followed for the determination of antibacterial and antioxidant activities of ZrO_2 and C-S-ZrO_2. The maximum COD, BOD, TOC, SO_4^{2-}, CO_3^{2-}, Cl^- and NO_3^-removal efficiencies of 77.3%, 87.6%, 97.7% 63.9%, 84.4%, 70.3% and 83.3 % at 120 min were obtained using C-S-ZrO_2 composite due to its higher surface area (80.165 m^2/g) and lower band gap (3.4 eV) compared with ZrO_2 (10.682 m^2/g). Carbon-sulphur co-doped ZrO_2 composite exhibited moderate antioxidant activity and increased peak current than other ZrO_2 based nanomaterials due to its highest surface area than ZrO_2 alone. The order of antibacterial activity of the nanomaterials against the *Salmonella typhi, Pseudomonas aeruginosa, Escherichia coli* is ZrO_2-C-S (15.40±1.11 mm, 25.10±1.80 mm, 20.03±2.50 mm) > C-ZrO_2 (9.45±2.65 mm, 11.18±0.33 mm, 15.45±3.25 mm) > S-ZrO_2 (7.52±1.55 mm, 12.45±0.11 mm, nil) >ZrO_2 (6.33±0.90 mm, 4.25±0.52 mm, nil). The experimental data best described by pseudo-first-order, followed by parabolic-diffusion and modified Freundlich models. The results showed that the synthesized C-S-ZrO_2 nanocomposite is highly efficient with excellent regenerative potential even after five cycles.

1. Introduction

Photocatalytic technology is one of the most eco-friendly advanced oxidation processes widely employed to treat complex industrial wastewater containing diverse organic pollutants (Ameta et al., 2018; Haq et al., 2021). In photocatalytic reaction, semiconductor metal oxides nanoparticles such as TiO_2, ZrO_2, WO_3, and ZnO have been extensively used particularly ZrO_2 due to its low cost, physical and chemical stability, excellent photocatalytic properties under excitation by UV radiation through absorption, scattering and reflection of light (Debnath et al., 2020; Mondal et al., 2017). ZrO_2 also referred to as zirconia is a white crystalline oxide of zirconium that occurs naturally and can be converted to other forms (Anandan et al., 2020; Renuka et al., 2021). The optical, mechanical, electrical, chemical and photocatalytic properties of this material (ZrO_2) make it suitable for different applications (Zarei et al., 2019). ZrO_2 exists in different phases, for instance at room temperature, a monoclinic crystal structure dominates and can be converted to tetragonal and cubic at higher temperatures

* Corresponding author at: Department of Chemistry, Federal University of Technology, PMB 65, Minna, Niger, Nigeria.
E-mail address: jimohtijani@futminna.edu.ng (J.O. Tijani).

https://doi.org/10.1016/j.clce.2022.100034
Received 22 March 2022; Received in revised form 18 May 2022; Accepted 3 June 2022

(Saraswathi et al., 2017). On the other hand, the band gap of ZrO_2 in the range of 5–7 eV is wide and hence limits its photocatalytic activity in the visible region.

To reduce this band gap, several strategies such as the incorporation of metallic and non-metallic elements, coupling with metal oxides have been adopted (Yadav et al., 2020). Doping using metal or non-metal alone has not been able to show any significant band gap reduction while metal doping (Fe doped ZrO_2) in most cases produced controversial photocatalytic activity results at both above UV and visible wavelengths. In most cases, metal doping result to thermal instability and increase of carrier-recombination centres (Kianfar et al., 2021; Mondal et al., 2017). The insolubility as well as secondary phase formation including surface aggregation has been listed as shortcomings of metal doped zirconia nanoparticles (Kianfar et al., 2021). There is also a problem of alteration of charged carrier diffusion length and narrow band bending, among others (Melchor-Lagar et al., 2020).

In view of these, non-metal doping or co-doping has been identified as a more viable strategy to reduce the band gap and hence improve the visible-light-driven activity of ZrO_2 (Danilenko et al., 2018; Zhang et al., 2019). Non-metal elements such as C, N, P, S, F, and B has been doped with metal oxides and enhanced photocatalytic activity was observed (Bhowmik et al., 2018; Fakhri et al., 2015; Renuka et al., 2021). Carbon and sulphur have a strong oxidizing ability and ionic radius of 170 and 180 pm, respectively (Sun et al., 2018). These values are greater than the ionic radius of oxygen (152 pm) which allows the two (non-metal) to displace oxide anion from ZrO_2 or occupy interstitial position respectively. More so, researchers have shown that effective band gap narrowing takes place as a result of the mixing of the 2p and 3p state of carbon and sulphur with the 2p state of oxygen in ZrO_2 (Kalampaliki et al., 2021). During doping, sulphur can exist either as anion (S^{2-}) or cation (S^{4+} or S^{6+}) and can readily replace Zr or O in the lattice layer of ZrO_2 (Agorku et al., 2015). Carbon also exists in the form of C^{4+} during chemical bonding. The effects of simultaneous co-doping phenomenon of carbon and sulphur on the photocatalytic activity of the synthesized metal oxides except ZrO_2 were also well documented and elucidated in the literature.

Physical and chemical methods of preparing ZrO_2 nanoparticles namely vapour phase, pyrolysis, hydrolysis, precipitation, hydrothermal and microwave plasma have certain shortcoming which makes it difficult to produce ZrO_2 nanoparticles in a large scale (Danilenko et al., 2018; Kalampaliki et al., 2021; Zhang et al., 2019). On the contrary, the green synthesis method of producing nanoparticles is simple and less complicated and operates at a very low temperature compared to other physical and chemical synthesis methods (Shinde et al., 2018). There is little or no information on the green synthesis of ZrO_2 nanoparticles using *Plumeria acuminata* leaves extract. *Plumeria acuminata* is a flowering cosmopolitan ornamentals plant that belongs to the family Apocynaceae and found mostly in the warm region of the world (Kaviya et al., 2020). Studies have shown that different parts of *Plumeria acuminata* are rich in phytochemical constituents such as alkaloids, tannins, phenols, flavonoids and others (Aghabeygi and Khademi-Shamami, 2018). These chemical components can perform the same function as toxic commercial reducing agents like $NaBH_4$, $LiAlH_4$, sodium citrate and others. Thus, the plant materials are readily available and affordable at little or no cost and can serve as a close substitute to commercial reducing agents thereby contributing to environmental sustainability (Kaviya et al., 2020).

Several reports on the synthesis of undoped and doped ZrO_2 nanoparticles have been reported. For instance, Fakhri et al. (2015) synthesised bare and carbon-doped zirconium dioxide (ZrO_2) nanoparticles via a simple sol-gel method and found that the doped ZrO_2 nanoparticles exhibited improved photocatalytic activity with 90% degradation efficiency of Amoxicillin and antibacterial activities (30×10^8 CFU of *Staphylococcus aureus*) than undoped counterpart within 120 min. Agorku et al. (2015) investigated the photocatalytic activity of N-S co-doped ZrO_2 for the degradation of indigo carmine and observed degradation efficiency of 98% and 66% for N-S ZrO_2 and pure ZrO_2 within 71 min. Anku et al. (2016) co-doped ZrO_2 with cobalt and carbon using a chemical method and applied the nanocatalyst for the degradation of indigo carmin and eosin Y dyes. The authors reported an increase in the percentage degradation from 21 to 88.8% after 180 min and increment was attributable to the introduction of the cobalt and carbon dopant onto the crystal lattice of ZrO_2 nanoparticles. Rajesh et al. (2020) doped Mg with ZrO_2 via an increase in the concentration of dopant from (0.2–0.8M) and the photocatalytic degradation efficiency was found to increase from 70 to 94% upon an increase in Mg dopant concentration. Similarly, Muhammad et al., (2021(the reference is now listed))doped ZrO_2 nanoparticles with chromium and apply (this should be applied and not apply) the nanocatalyst for the degradation of methylene blue under UV light and found that the degradation efficiency of the catalyst decreased from 78.41 to 73.07% upon an increase in the amount of dopant from 1 to 3 g.

In this study, the photocatalytic performances of the synthesised nanocatalyst were tested on organic dyes in real dyeing wastewater. It should be mentioned that the total collapse of most textile industries in Nigeria have led to the printing of clothing/fabrics material with different dyes by various ethnic groups (Kaliraj et al., 2019). This indigenous industry require no special skills in their operations and a large volume of water and approximately 50–65% of organic dyes are used during the dyeing process and 10–15% of the dyes stuff not properly fastened with fabrics get released as wastewater into the environment (Aneyo et al., 2016). These activities are widely recognized as one of the root cause of environmental pollution because the wastewater contains complex organic aromatic compounds and colors that can cause several health problems (Kaliraj et al., 2019). The effects of exposure to such wastewater includes damage aquatic organisms, skin irritation, diarrhoea, allergic, vomiting, bladder cancer depending on the length of time of exposure and concentration (Zhang et al., 2019).

Nevertheless, to the best of our knowledge, this study report for the first time photocatalytic, electrochemical, antibacterial and antioxidant properties of a novel carbon-sulphur co-doped zirconia nanocomposite. ZrO_2 nanoparticles and carbon-sulphur co-doped ZrO_2 nanocomposite were synthesized by green synthesis method. Subsequently, the synthesized materials were analyzed using several characterization tools to ascertain their morphology, microstructures, elemental composition, crystallinity, phase structure, surface area. The photocatalytic/adsorptive properties of the synthesized carbon-sulphur co-doped ZrO_2 nanoparticles on local dyeing wastewater in the presence or absence of sunlight was investigated. The electrochemical behaviour of the nanomaterial was assessed using cyclic voltammetry. The antibacterial potential of the prepared nanomaterials was also evaluated using Agar well diffusion method. The *in vitro* antioxidant activity of the zirconia-based nanomaterials was assessed using 2,2-Diphenyl-1-picrylhydrazyl (DPPH) and 2,2'-azinobis-(3-ethylbenzothiazoline-6-sulfonic acid (ABTS) methods respectively. The recyclability and stability behaviour of the zirconia-based nanomaterial was also investigated.

2. Materials and methods

2.1. Chemicals and reagents

The following chemicals/reagents: Zirconyl chloride octahydrate (98%), sodium hydrosulphide (>99.5%) and Polyvinylpyrrolidone were purchased from Sigma Aldrich. *Plumeria acuminata* leaves were collected from the premises of the Federal University of Technology, Bosso, Minna. The leaves were washed thoroughly to remove dirt and sand particles, after which it was allowed to dry at room temperature for two weeks. The sample bottle was washed thoroughly with Nitric acid (70%), rinsed with double distilled water and allowed to dry to avoid contamination of the sample. The wastewater was collected in a dark sample bottle from a local (indigenous) dyeing industry in Bosso, Minna,

transported to the laboratory and stored in the fridge at a temperature of 4°C until further use.

2.2. Preparation of Plumeria acuminata leaves extract

The dry leaves of *Plumeria acuminata* were milled into powdery form and 50 g was washed into 1 L volumetric flask followed by the addition of distilled water. The mixture was allowed to stand for 24 h after which the solution was filtered. The obtained extract was labelled appropriately and stored in an airtight container until further use.

2.3. Green Synthesis of zirconium oxide nanoparticles

The green synthesis of ZrO_2 nanoparticles was carried out using the modified method described by Dawoud et al., (2020). In brief, 40 cm^3 of 0.5 M zirconyl chloride octahydrate solution was added into *Plumeria acuminata* aqueous leaves extract in a 100 cm^3 beaker dropwise and stirred at 500 rpm on a magnetic stirrer for 30 min. After which the pH of the solution was adjusted to 9 with 0.5 M NaOH solution and light and deep yellow precipitates were formed and then subjected to centrifugation at 1000 rpm. The clear upper layer liquid was decanted and the precipitates were washed thoroughly with deionized water to remove all impurities. Thereafter, the sample was oven-dried at 80°C for 3 h and later transferred into a furnace before calcination at 500°C for 2 h to produce ZrO_2 nanoparticles.

2.4. Preparation of carbon-sulphur co-doped zirconium oxide nanocomposites

One-pot green synthesis adopted for the preparation of carbon-sulphur co-doped zirconium oxide nanocomposite can be described as follows: 10 cm^3 of 3wt% polyvinylpyrrolidone and 3wt% sodium hydrosulphide were simultaneously added to the equal mixture (40 cm^3) of 0.5 M zirconyl chloride octahydrate solution and *Plumeria acuminata* aqueous leaves extract in a 100 cm^3 beaker and stirred at 500 rpm for about 2 h. The mixture was centrifuged at 1000 rpm for 15 min; oven-dried at 80°C for 3 h and calcined at a temperature of 500°C in a furnace for 2 h. A similar procedure was repeated for the preparation of carbon-doped ZrO_2 nanocomposites but in the absence of 3wt% sodium hydrosulphide. Likewise, the same approach was employed for the synthesis of sulphur doped ZrO_2 nanocomposites without the addition of 3% polyvinylpyrrolidone (Fakhri et al., 2015; Wahba et al., 2020).

2.5. Characterization of zirconium oxide nanoparticles and nanocomposites

The morphology of the prepared samples was obtained using Zeiss Auriga High-Resolution Scanning Electron Microscope (HRSEM) fitted with a secondary electron detector and Energy Dispersive X-ray spectroscopy (EDS). The EDS was done by adjusting the measurement angle to 150°C and voltage to 20 kV respectively. High-Resolution Transmission Electron Microscopy images model Zeiss Auriga operated at an acceleration voltage of 20 kV was used to examine the microstructure and particle size. UV-Visible Spectroscopy, in this case, the Shimadzu UV 1800 was used to determine the wavelength of adsorption. The specific surface area of the synthesized nanoparticles and nanocomposite were determined using NOVA 2400e by applying N_2 as an absorbate on a micrometre ASAP 2020 chemisorption surface area analyzer.

2.6. Determination of physicochemical parameters of local dyeing wastewater

The Shimadzu UV 1800 was used for the identification of different dyes in wastewater scanned in the wavelength range of 200–800 nm. 1 cm^3 of the wastewater was added into a cuvette followed by the addition of 1 cm^3 distilled water and then scanned in the range of 200–800 nm at scanning speed rate of 50 nm/min. Bioassay and gravimetric methods were employed for the determination of BOD and TDS respectively. Then, a closed reflux colorimetric method was followed for the determination of COD. The TOC value was determined using non-dispersive infrared analyzer (model 8869) from the amount of converted non-purging bonded carbon to CO_2 (Bailón-García et al., 2017). The argentometric method was used for the estimation of chloride ion concentration in the wastewater. A pH meter probe standardized with Buffer 4 and 7 was used for the pH determination. A multi-parameter water quality meter was utilized for the estimation of the alkalinity level of the wastewater. The colorimetric method was used for the determination of nitrate and sulphate. The level of carbonates in the wastewater was determined using the Direct Titrimetric method.

2.7. Adsorption experiment

The adsorption experiment of the synthesized undoped, mono-doped and co-doped ZrO_2 nanoparticles was evaluated in the dark using the magnetic stirrer. 0.5 g of the undoped catalyst (ZrO_2) was added to the 50 cm^3 of dyeing wastewater in a 250 cm^3 corked conical flask kept in the dark under magnetic stirring at 500 rpm for 2 h. 5 cm^3 of the wastewater were taken at regular time interval of 30 min and filtered using Whatman No. 1 filter paper. The reduction in the level of COD, BOD, TOC SO_4^{2-}, CO_3^{2-}, NO_3^-, Cl^- by ZrO_2 alone was evaluated. The procedure was repeated for carbon-doped ZrO_2, sulphur doped ZrO_2 and carbon-sulphur doped ZrO_2 nanocomposites.

2.8. Photocatalytic experiment

The photocatalytic experiments of the synthesized undoped, mono-doped and co-doped ZrO_2 nanoparticles were evaluated using a 250 cm^3 capacity photoreactor with a magnetic stirrer. Natural sunlight was used as an irradiation source with average daily intensity of $1.75 \times 10^{\wedge 5}$ Lux units or 252.92 W/m^2 at ambient temperature of 35°C. 0.5 g of the nanocatalyst (ZrO_2 alone) was added to 50 $cm^3$of the local dyeing wastewater. The solution was kept in dark under magnetic stirring of the wastewater effluent for 30 min to establish the adsorption-desorption process. Thereafter, the mixture in a reactor was exposed to natural sunlight and stirred continuously with stirring speed 500 rpm for 2 h. A sampling of 5 cm^3 of the wastewater was done at regular time interval of 30 min and filtered using Whatman No. 1 filter paper. The photocatalytic degradation of the local dyeing wastewater using the nanocatalysts was evaluated by measuring the level of BOD, COD, TOC and other parameters (SO_4^{2-}, CO_3^{2-}, NO_3^-, Cl^- and pH). The procedure was repeated for carbon-doped ZrO_2, sulphur doped ZrO_2 and carbon-sulphur doped ZrO_2 nanocomposites.

2.9. Electrochemical studies

Electrochemical studies (Cyclic Voltammetry measurement) were investigated in an electrode cell using a Solartron workstation at 25 °C. A working screen-printed carbon electrode (SPCE) and Ag/AgCl was used as standard reference and a solution of 0.2 M H_2SO_4 was used as an electrolyte. The cyclic voltammetry data were recorded in the potential range of -0.3–0.6 V with a scan rate of 50 mV/s.

2.10. Antibacterial activity of ZrO_2 nanoparticles and composites

ZrO_2 nanoparticles and its composites were screened against *Escherichia coli, Pseudomonas aeruginosa, Salmonella typhi* obtained from the Vaccine Laboratory of Centre for Genetic Engineering and Biotechnology, Federal University of Technology Minna, Niger State, Nigeria. The bacteria were pre-cultured in a nutrient broth overnight using a

rotary shaker at 37°C. Thereafter, each strain was adjusted at a concentration of 10^8 cells/mL using 0.5 McFarland standards (Bhalodia and Shukla, 2011). The modified Agar well diffusion method reported by Daoud et al. (2015) was used to establish the antibacterial activities of the nanoparticles and its composites. Nutrient agar Petri dishes were swabbed with 3 h old broth culture of the respective bacterial isolates. Wells were made using a sterile cork borer (6 mm in diameter) into agar plates containing inoculums. Then, 100 mL of 400 mg/mL of the nanoparticles was added to the respective wells. The plates were allowed to stay on the bench for 30 min to let the sample diffusion properly into the agar. Then, the plates were incubated at 37°C for 18 h. Antibacterial activity was determined by measuring the zone of inhibition after the incubation period minus the diameter of the cork borer (6 mm). Tween 80 at a concentration of 10% was used as negative control while chloramphenicol (1 μg/mL) was used as the positive control.

2.11. Antioxidant activity of ZrO_2 nanoparticles and composites

Herein, 2,2-Diphenyl-1-picrylhydrazyl (DPPH) radical-scavenging activity of ZrO_2 based nanomaterial against DPPH radical were assessed according to the method described by Gordon et al. (2001) with slight modifications. Briefly, 1 mL of the nanomaterial (0.01 mg/mL) was mixed with 4 mL of 0.005 mg/ml DPPH methanol solution. The reaction mixture was vortexed thoroughly and left in the dark at room temperature for 30 min. The absorbance of the mixture was measured at 517 nm. Garlic acid was used as a reference. The ability to scavenge DPPH radical was calculated by Eq. (1).

$$DPPH\ radical\ scavenging\ efficiency\ (\%) = \frac{Abs\ control - Abs\ sample\ Abs\ control}{Abs\ control} \times 100 \quad (1)$$

where Absorbance of control is the absorbance of DPPH radical in methanol without extract. All determinations were performed in triplicate ($n = 3$).

Also, 2,2'-azinobis-(3-ethylbenzothiazoline-6-sulfonic acid (ABTS) radical scavenging assay of the nanomaterial was carried out following the modified method described by Gião, et al. (2007). The stock solutions included 7 mM ABTS solution and 2.4 mM potassium persulfate solution. The working solution was then prepared by mixing the two stock solutions in equal quantities and allowing them to react for 14 h at room temperature in the dark. The solution was then diluted by mixing 1 mL ABTS solution with 60 mL methanol to obtain an absorbance of 0.706 ± 0.01 units at 734 nm using a spectrophotometer. Fresh ABTS solution was prepared for each assay. Nanomaterial (1 mL) was allowed to react with 1 mL of the ABTS solution and the absorbance was taken at 734 nm after 7 min using a spectrophotometer. The ABTS scavenging capacity of the nanomaterial was compared with that of ascorbic acid and percentage inhibition was calculated using Eq. (2).

$$ABTS\ radical\ scavenging\ efficiency\ (\%) = \frac{Abs\ control - Abs\ sample\ Abs\ control}{Abs\ control} \times 100 \quad (2)$$

Where, Absorbance of control is the absorbance of ABTS radical in methanol. All determinations were performed in triplicate ($n = 3$).

2.12. Regeneration and reusability

For the reusability study, the recovered adsorbent and nanocatalysts at the end of the adsorption and photocatalytic process were dried and reused for the degradation of BOD, COD and TOC at the optimum operating conditions. Particularly, 10 mg/L each for the ZrO_2, ZrO_2-C, ZrO_2-S and ZrO_2-C-S were added into the dyeing wastewater and stirred continuously at 500 rpm for 1 h. Using 1.0 M of NaOH and HCl, the desorption examination was conducted to ascertain the stability and reusability under adsorption and photocatalytic methods. The regeneration efficiency (RE) was determined using the expression in Eq. (3) (Song et al., 2022).

$$RE(\%) = \frac{Qr}{Qo} \times 1000 \quad (3)$$

in which Q_r and Q_0 in mg/g represent the removal capacity of the regenerated and the fresh the ZrO_2, ZrO_2-C, ZrO_2-S and ZrO_2-C-S.

3. Results and discussion

3.1. Characterization of ZrO_2 based nanomaterial

3.1.1. HRSEM analysis

HRSEM was employed to examine the morphology of the prepared ZrO_2 based nanomaterial and their corresponding micrographs are shown in Fig. 1.

HRSEM image of pure ZrO_2 nanoparticle shown in Fig. 1(a) revealed the formation of sparsely distributed aggregated and spherical particles. Also, the HRSEM image of the 3% sulphur-ZrO_2 nanoparticle in Fig. 1(b) demonstrated the presence of well distinct homogenously distributed and agglomerated spherical particles. This degree of aggregation could be attributed to the introduction of sulphur onto the lattice layer of ZrO_2 nanoparticles. The dispersion of sulphur particles on the ZrO_2 matrix can be linked to the displacement of oxygen in ZrO_2 by sulphur due to the greater ionic radius of sulphur (180 pm) than oxygen (80 pm). The HRSEM micrograph of 3% carbon-doped ZrO_2 shown in Fig. 1(c) revealed the presence of well-dispersed and aggregated particles compared to pure ZrO_2 nanoparticles alone. The slight change in morphological properties may be attributed to the carbonaceous material introduced onto the ZrO_2 matrix and the substitution of oxygen by carbon-based on ionic radius mechanism. The ionic radius of carbon (170 pm) is also higher than oxygen (80 pm) and thus allow easy displacement of oxygen in ZrO_2 by carbon. Typically, the HRSEM image of 3% carbon-sulphur co-doped ZrO_2 in Fig. 1(d) revealed the presence of spherical and irregular hexagonal shape due to the co-doping phenomenon of carbon-sulphur on the lattice layer of ZrO_2. Arjun et al. (2020) observed a phase change from cubic phase to spherical phase upon a change in dopant concentration from 0 to 0.05 % for copper doped ZrO_2 nanoparticles prepared via sol-gel method.

3.1.2. XRD analysis of mono and co-doped zirconium oxide nanoparticles

XRD pattern of ZrO_2, ZrO_2 doped with 3wt% sulphur, ZrO_2 doped with 3wt% carbon and –3wt% carbon- sulphur doped ZrO_2 is presented in Fig. 1e. The XRD spectra in Fig. 1e(a) revealed sharp diffraction peaks at 2 theta values of 30.224°, 50.924° and 62.855° which corresponds to crystal plane (011), (310), and (231) respectively. These peaks are characteristic properties of ZrO_2 nanoparticles with a tetragonal phase according to JCP2_79-1766 (Renuka et al., 2021). The formation of sharp and intense diffraction peaks confirmed that the synthesized ZrO_2 is crystalline, which is in agreement with Kurakaran et al. (2014) who employed an aqueous gelation method to prepare tetragonal phase ZrO_2 nanoparticles. Non-detection of other peaks in the undoped ZrO_2 confirmed formation of pure ZrO_2 nanoparticles.

On the other hand, the XRD spectra of 3wt% sulphur doped ZrO_2 (Fig. 1e(b)) shows three sharp peaks at 2 theta values of 30.241°, 32.978° and 62.855° which correspond to the crystal plane (011), (200) and (231) respectively of a characteristic orthorhombic phase according to JCP2_83-0809 card. The phase change may be linked to the sulphur addition based on the interstitial substitution of Zr^{4+} by either S^{6+} or S^{4+} that inhibited the growth of ZrO_2 particles. The intensity of the diffraction peaks with miller indices (200) observed for pure ZrO_2 alone decreased remarkably due to the sulphur addition in the matrix (Bharathi et al., 2020). The phase change observed in this work corroborated the findings of Szatmáry et al. (2011) who doped sulphur with titanium oxide to produce rutile instead of anatase phase at a temperature above 500°C. Similarly, Malyi et al. (2011) studied the effect of

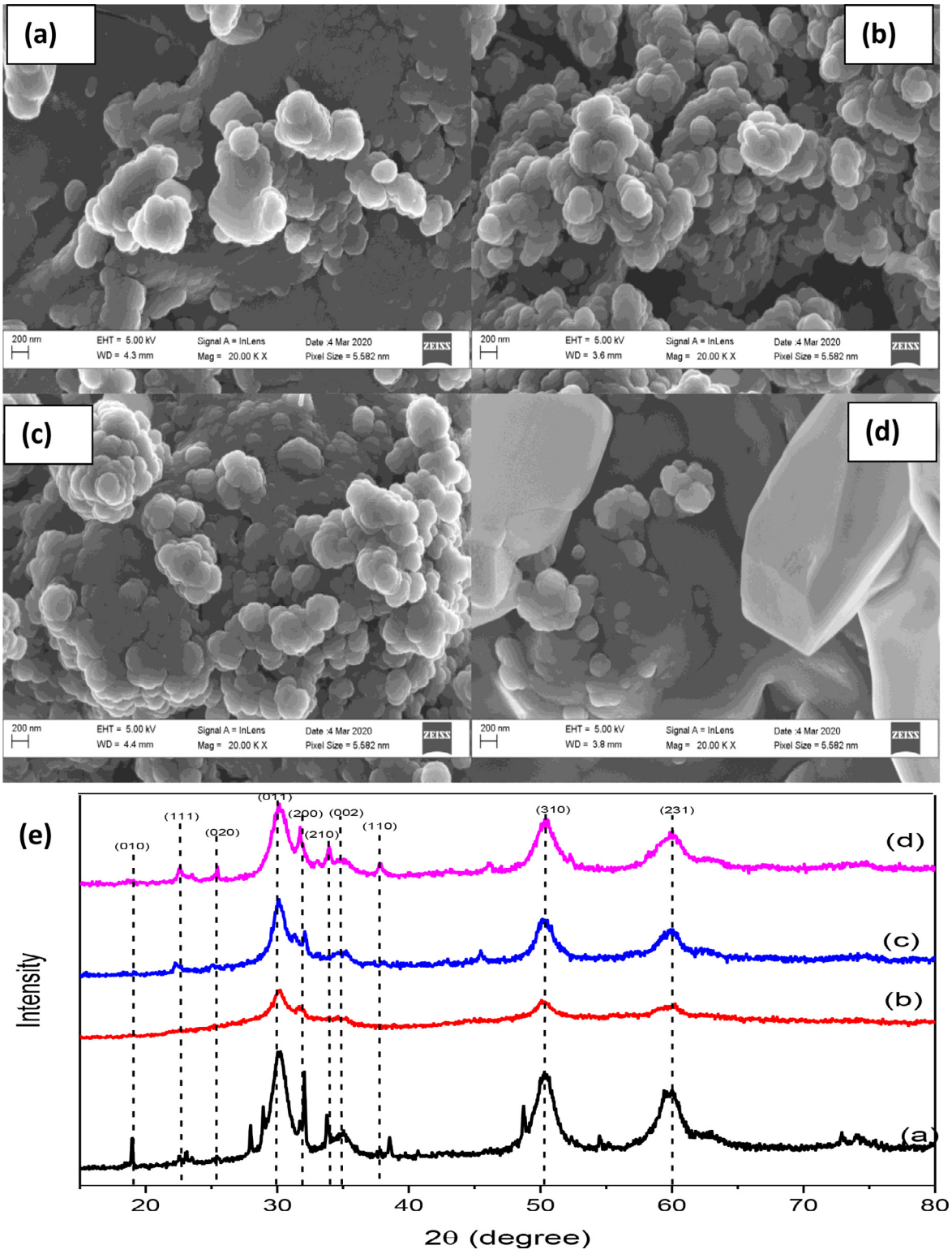

Fig. 1. HRSEM Image of (a) pure ZrO_2 (b) ZrO_2 doped with 3% sulphur (c) ZrO_2 doped with 3% carbon (d) ZrO_2 co-doped with 3% carbon-sulphur and (e) XRD pattern of ZrO_2 based nanomaterials ((a) ZrO_2; (b) ZrO_2 doped with 3% sulphur; (c) ZrO_2 doped with 3% carbon and (d) ZrO_2 co-doped with 3% carbon and sulphur).

sulphur impurity on the stability of cubic Zirconium oxide and its interface with water and observed a phase change from cubic phase to tetragonal upon the addition of sulphur to the sample matrix.

The XRD spectra for 3wt% carbon-doped ZrO_2 nanoparticle (Fig. 1e(c)) also revealed more sharp peaks than 3wt% sulphur doped ZrO_2 nanoparticles. These peaks were assigned to the tetragonal phase. This implies that the addition of carbon did not influence the phase of ZrO_2 nanoparticles because carbon diffused onto the pores of ZrO_2 nanoparticles due to its smaller ionic radius (170 pm) than sulphur (180 pm). None transformation of tetragonal phase of ZrO_2 to orthorhombic due to incorporation of carbonaceous material may be linked to equal number of four outer most electrons in Zr^{4+} and C^{4+} respec-

tively. In addition, studies have shown that non-metals such as nitrogen and carbon can generate oxygen vacancy and thus, act as a stabilizer to tetragonal ZrO_2 nanoparticles (Bailón-García et al., 2017). Non-distortion of the tetragonal phase of ZrO_2 had earlier been reported by Fakhri et al. (2015) who doped carbon with zirconium oxide and revealed a tetragonal phase according to (JCPD_79-1771) with no evidence of phase change. The XRD spectra of 3wt% carbon-sulphur co-doped ZrO_2 nanocomposites (Fig. 1e(d)) revealed six prominent peaks at 2 theta values of 30.224°, 32.987°, 34.256°, 36.982°, 51.789° and 60.855° which correspond to crystal plane (011), (200), (210), (110), (310) and (231) respectively. Also, two smaller/less prominent peaks appeared at 2 theta values of 20.959° and 27.490° may be due to the doping effect of carbon on ZrO_2 nanoparticles. Also, the co-doping effect resulted in the formation of mixed-phase (tetragonal and orthorhombic) of ZrO_2 nanoparticles (Anandan et al., 2020). This implies that the mono and co-doping influence phase change. Comparatively, more diffraction peaks were observed in the ZrO_2 co-doped with carbon and sulphur than the mono and undoped ZrO_2. Also, diffraction peaks noticed at 2 thetha values of 50.924° (310) and 62.855°(231) were sharp and more intense than that noticed in Fig. 1e (b) due to the carbon diffusion effects than sulphur.

According to the Debye-Scherrer equation(Egbosiuba and Abdulkareem, 2021)., the calculated crystallite size of the pure ZrO_2 nanoparticles was 20.03 nm, ZrO_2 doped with sulphur was 17.51 nm, ZrO_2 doped with carbon was 16.03 nm, while the co-doped ZrO_2 with carbon-sulphur was 12.40 nm. The doping phenomenon influenced the crystallite size and the obtained size also depends on the nature of the dopants. It can be noticed that the single ZrO_2 grain size is larger than that of the composites containing ZrO_2, implying that the introduction of the dopants significantly improved the dispersion of ZrO_2, which may enhance the adsorptive and photocatalytic performance.

3.1.3. HRTEM/SAED analysis of ZrO_2 based nanomaterial

The microstructure and crystalline nature of the samples were examined using HRTEM Zeiss Auriga and their corresponding images at high and low magnification and SAED pattern are represented as Fig. 2.

Fig. 2(a and a_1) show the presence of tiny but highly agglomerated particles with lattice fringes, which suggest that the material synthesised is crystalline. Fig. 2(b and b_1) show the formation of more densely distributed spherical particles with lattice fringes, which is also characteristic of crystalline material. This slight change in property may be attributed to the presence of sulphur (dopant) in the sample. The appearance of densely distributed spherical nanoparticles compared to ZrO_2 alone further suggest phase transformation as earlier observed in the XRD result in Fig. 1e(b).

In the case of Fig. 2(c and c_1), tiny and highly agglomerated particles with little lattice fringes were observed. A slight reduction in crystallinity of the material may be due to the presence of carbon acting as a dopant. This justified the non-phase transformation revealed in the XRD pattern in Fig. 2(c) and evidence of the formation of a single-phase (Reddy et al., 2020). Furthermore, Fig. 2(d and d_1) reveal the presence of tiny and agglomerated particles with an increase in lattice fringes which indicates an increase in crystallinity. This increase in crystallinity was linked to the co-doping effect mechanism of sulphur and carbon on the host matrix (ZrO_2). Also, the increase in lattice fringes corresponds to the surface exposure of the closely packed (011) crystal plane of ZrO_2 as indicated by Ahmed et al. (2021) who reported controlled green synthesis of ZrO_2 nanoparticles with tailored size morphology using Enterobacter species.

The SAED image in Fig. 2(a_2) revealed the presence of a tiny, bright, sharp and intense ring pattern which shows that the material is highly crystalline. The ring pattern corresponds to the number of diffraction peaks observed in the XRD analysis in Fig. 1e(a). Fig. 2(b_2) revealed the presence of a bright dotted ring pattern which indicates the presence of single crystalline material. The change in ring pattern from a sharp bright ring to a bright dotted ring revealed the influence of sulphur in the host matrix. The formation of a single crystalline phase is an indication of phase change observed in ZrO_2 from tetragonal to orthorhombic in 3wt% sulphur doped ZrO_2 nanoparticles. Fig. 2(c_2) demonstrates the presence of a bright dotted rings pattern indicating that the material is crystalline and the crystallinity was linked to the presence of carbon acting as a dopant.

Fig. 2(d_2) revealed the presence of a ransom dotted and unclear ring pattern, this indicates that the material is polycrystalline, the change in ring pattern from a bright dotted ring to a dotted and unclear pattern indicates formation of a mixed phase and evidence of carbon-sulphur co-doping effect (Shinde et al., 2018). These changes in a ring pattern correspond with the change in crystalline phase as shown in the XRD pattern in Fig. 1e(d).

3.1.4. EDS analysis of ZrO_2 based nanomaterial

EDS analysis (elemental composition) was carried out and the corresponding weight percentage (elemental composition/distribution of the sample structure) obtained are shown in Fig. S1(supplementary information). For the ZrO_2 nanoparticles, the following elements were detected (Zr, and O) with Zr the most prominent and abundant. Also, the presence of O confirms the sample is ZrO_2 nanoparticles. For the ZrO_2 doped with 3 % sulphur, Zr, S, and O were detected. Zr remains the most dominant while the presence of sulphur was attributed to the sodium hydrosulphide used as a dopant. The O might be from the phytochemical constituents in the leaves extract of *Plumeria acuminate* or zirconium salt precursor.

The ZrO_2 doped with 3wt% carbon revealed the presence of Zr, C and O. The amount of Zr was still dominant while C is present as the dopant in the sample matrix originating from polyvinylpyrrolidone used. For the co-doped ZrO_2 with sulphur and carbon, Zr, C, S and O were detected. The amount of Zr slightly reduced due to the co-doping effect. The presence of S and C confirmed successful doping of ZrO_2 with the two elements

3.1.5. UV-visible analysis of ZrO_2 based nanomaterial

UV-Visible analysis was carried out to determine the absorption band (Fig. 3(I)) and the band gap energy of ZrO_2 based nanomaterial displayed as the Tauc plot in Fig. 3(II).

The UV-visible spectrum of ZrO_2 revealed an absorption band at 302 nm. This corresponds with the findings of Anku et al. (2016) who observed ZrO_2 nanoparticles in the wavelength range of (300–366 nm). Both 3wt% carbon doped ZrO_2 with and ZrO_2 doped with 3wt% sulphur showed an absorption band at 350 and 345 nm respectively while the UV-visible spectrum of C-S-ZrO_2 composite has an adsorption band at 360 nm. A slight shift in the adsorption edge of C-ZrO_2 compared to ZrO_2 alone may be linked to the quantum confinement. This shift in the adsorption band edge towards the visible region may suggest the prevention of electron-hole pairs from the valence band to the conduction band of ZrO_2 nanoparticles. This is evidence of an increase in photocatalytic efficiency from the mono doped to the co-doped ZrO_2 nanomaterials. Eq. (4) connects absorption coefficient and photon energy

$$(\alpha h\nu)^2 = C\left(h\nu - E_g\right) \tag{4}$$

where C is a constant derived from $\alpha = \frac{A}{d}$ while A is the absorbance and d is the thickness of the sample in the UV-Visible cell.

The band gap energy of the synthesised nanomaterials were obtained by extrapolating the linear portion of the graph $(\alpha h\nu)^2$ versus hv shown in Fig. 3(II). According to Fig. 3(II)(a), the band gap energy of pure ZrO_2 nanoparticles is approximately 5.2 eV, which correspond to the value reported in the literature for a typical ZrO_2 (Dharr et al., 2020; Majedi et al., 2015). The band gap of ZrO_2 doped with 3wt% carbon was 3.75 eV, ZrO_2 doped with 3wt% sulphur had a band gap of 4.1 eV while the ZrO_2 co-doped with 3wt% carbon-sulphur revealed a band gap of 3.4 eV. The Tauc plot indicates a significant reduction in the band gap of ZrO_2 nanomaterial from (5.2-3.4 eV) from the mono doping to co-doping activity. The decrease in the band gap energy is an indication of

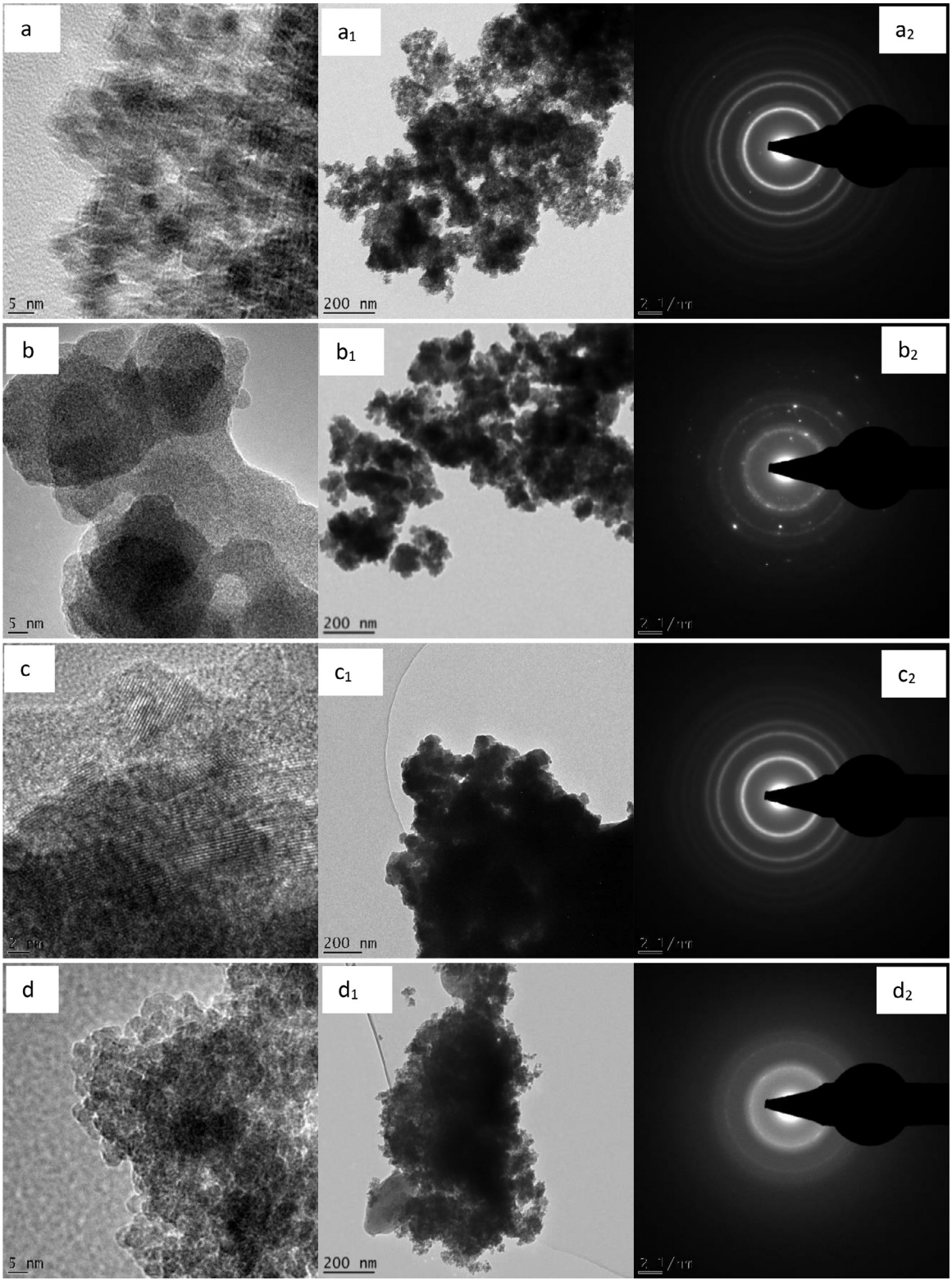

Fig. 2. HRTEM images at low and high magnification and selected SAED pattern of (a) pure ZrO_2 (b) 3% sulphur doped ZrO_2 (c) 3% carbon doped ZrO_2 (d) 3% carbon-sulphur doped ZrO_2.

lattice distortion and orbitals hybridization of 4d states in Zr with mixture 2p and 3p states in carbon and sulphur during the co-doping effect. The reduction in band gap is an indication of the suppression of the electron-hole pairs recombination rate for typical ZrO_2 nanoparticles. The reduction further suggests the synthesis of enhanced visible-light-driven ZrO_2 based nanocatalysts. This is in agreement with the literature and corresponds to the findings of Wahba et al. (2020).

3.1.6. Photoluminescence properties

The photoluminescence behaviour of the synthesised ZrO_2 based nanomaterials provided in Fig. 3(III) was studied at room temperature so

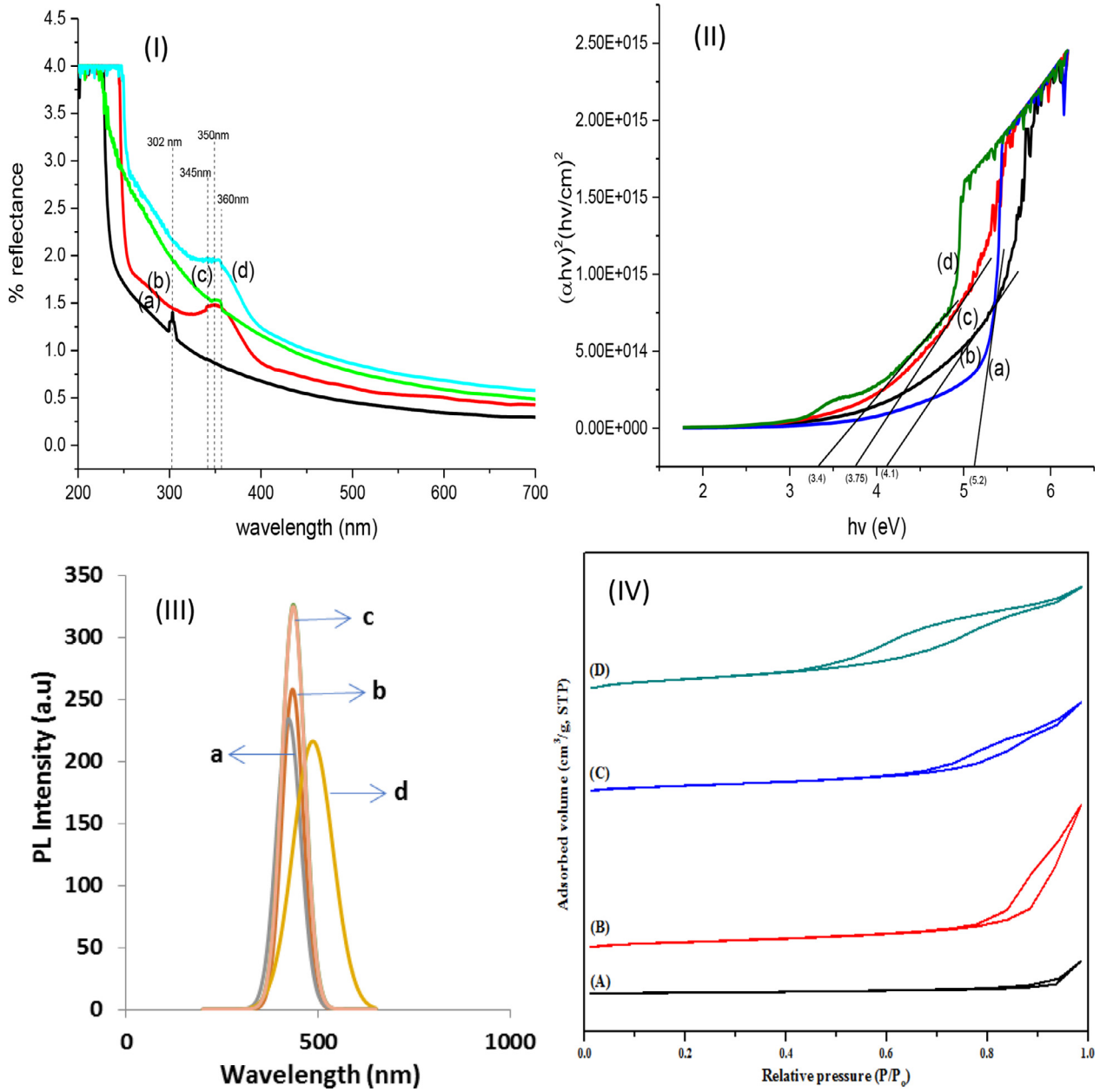

Fig. 3. (I) UV-visible spectra of ZrO_2 based nanomaterials ((a) ZrO_2 (b) ZrO_2 with 3% sulphur (c) ZrO_2 3% carbon and (d) ZrO_2 with 3% sulphur-carbon); (II) Tauc plot of ZrO_2 based nanomaterials ((a) ZrO_2 (b) ZrO_2 with 3% sulphur (c) ZrO_2 with 3% carbon and (d) ZrO_2 with 3% sulphur-carbon); (III) The PL spectra of ZrO_2 based nanomaterials ((a) ZrO_2 alone (b) ZrO_2 with 3% sulphur (c) ZrO_2 with 3% carbon and (d) ZrO_2 with 3% sulphur-carbon) and (IV) BET spectra of ZrO_2 based nanomaterials ((A) pure ZrO_2 (B) ZrO_2-S (C) ZrO_2-C (D) ZrO_2-S-C).

as obtain information on the defect energy states due to the addition of carbon and sulphur. The undoped ZrO_2 nanoparticle emitted at a lower wavelength (400 nm) and the peak intensity of ZrO_2 alone is lower than mono and co-doped ZrO_2 nano-based material. This is evidence of defects of oxygen or zirconium vacancy in ZrO_2. Other researchers ascribed the PL peak noticed at 400 nm to Zr vacancies based on the band edge emission and free-exciton recombination (Majedi et al., 2015, Singh and Nakate, 2014).

The doping of carbon and sulphur atoms onto the lattice layer of ZrO_2 nanoparticles may create further defect states which were corroborated with the appearance of peaks at a longer wavelength region. Fig. 3(III) also indicates a narrow (for samples a, b, c) and wide emission spectrum (sample d) in the range of 350–650 nm. The narrow emission band further demonstrates surface defects and oxygen vacancies.in ZrO_2 nanoparticles. High band gap energy of 5.2 eV for the as-synthesized nano-ZrO_2 particles corroborated the existence of high amounts of surface defects. The wide band and the substantial red shift for C-S-ZrO_2 nanocomposite relative to ZrO_2 alone strongly suggest the involvement of fluorescence extrinsic states and the existence of the material in two phases (tetragonal and orthorhombic). The systematic shifting to a longer wavelength due to the co-doping phenomenon suggests the existence of a synergetic effect between the two dopants.

3.1.7. BET analysis of ZrO_2 based nanomaterials

The BET analysis was carried out to determine the surface areas of the synthesized ZrO_2 nanomaterials. The surface area, pore diameter and pore volume including the adsorption-desorption curve are shown in Table 1 and Fig. 3(IV), respectively.

Table 1
BET analysis of ZrO_2 based nanomaterial.

Sample	Surface area (m^2/g)	Pore diameter (nm)	Pore volume (cc/g)
ZrO_2	10.682	16.070	0.157
ZrO_2.S	24.824	8.854	0.133
ZrO_2.C	52.637	5.293	0.127
ZrO_2.S-C	80.165	4.053	0.061

According to the IUPAC classification, all the samples in Fig. 3(IV) except ZrO_2 alone exhibits type IV adsorption isotherm, a typical mesoporous material (Zhang et al., 2020). However, the degree of mesoporosity differs and depends on the nature of dopants. The existence of several mesoporous on the carbon-sulphur-ZrO_2 is an indication of more active sites and high adsorptive capacity. This is beneficial to the synergetic adsorption and photocatalytic reaction. Typically, Fig. 3(IV) indicates that the ZrO_2 co-doped with carbon-sulphur has the highest surface area (80.165m^2/g) followed by ZrO_2-C (52.637m^2/g) and ZrO_2-S (24.824m^2/g) while pure ZrO_2 (10.682 m^2/g) has the least surface area. The surface area of sulphur doped ZrO_2 is twice that of pure ZrO_2 and carbon-doped ZrO_2 is five times the pure ZrO_2 while the carbon-sulphur co-doped ZrO_2 is eight times pure. The surface area and pore volume of sulphur-ZrO_2, carbon-ZrO_2 and carbon-sulphur-ZrO_2 increased significantly due to the dispersed stacking of carbon and sulphur particles on the surface of ZrO_2. Hence, the ZrO_2 co-doped with carbon-sulphur have a higher tendency to enhance a visible-light-driven photocatalysis and adsorption process than others based on the higher surface area. The increase in surface area from the mono dope to the co-doped can be attributed to the influence of the dopant on the sample matrix. The pore diameter decreases on the incorporation of the dopant from the mono-doped to the co-doped and could also be linked to the dispersion of the dopants on the pores of the ZrO_2 nanomaterial (Yousefi et al., 2018). The adsorption isotherm of pure ZrO_2 did not show any evidence of mesoporosity. On the introduction of sulphur dopant, the adsorption isotherm revealed a mild mesoporosity. Also, the carbon-doped ZrO_2 nanoparticles revealed a slightly higher mesoporosity than sulphur-doped ZrO_2. The carbon-sulphur co-doped ZrO_2 indicates a higher mesoporosity adsorption isotherm. This increase in mesoporosity could be linked to the simultaneous displacement or substitution of O_2 in the ZrO_2 matrix by carbon and sulphur.

3.2. Physico-chemical analysis of local dye wastewater before photocatalytic degradation/adsorption studies

The adsorption band of the local dyeing wastewater was examined using the UV-visible spectrometer and the adsorption spectrum is represented in Fig. S2, while the result of the physicochemical parameters of the dyeing wastewater is shown in Table S1. The result reveals that the dye wastewater adsorbs near and within the visible region at a wavelength of 270 and 600 nm, respectively. This adsorption band fall within the adsorption range reported for azo dyes (270–600 nm) (Aneyo et al., 2016). Overall, Table S1 reveals high values of COD, TOC and BOD, an indication of the presence of oxidizable organic and inorganic dyes (Aghabeygi and Khademi-Shamami., 2018). The COD level is 1448 mg/dm^3 against the WHO/NIS standard of 50 mg/dm^3/500 mg/dm^3. This suggests a high level of biological resistant substances in water. BOD level is 670 mg/dm^3, which is above the tolerable limit of 50 mg/dm^3, an indication of a very limited amount of oxygen for aquatic organisms in wastewater. While TOC value is 402 mg/dm^3 as against the recommended limit of 5 mg/dm^3 which mean a very high level of dissolved organic compounds in the wastewater. The nitrate, sulphate, pH and carbonate values were considerably higher than the WHO/NIS permissible limit. The pH value at 8.70 is slightly alkaline due to the usage of different types of basic dyes and the nitrogen content in the dye and the use of the strong base in the dyeing process. The nitrate concentration is 58.8, about six times higher than the recommended value. This can cause blue baby syndrome in infants and pregnant women. The sulphate level is 1634.90 mg/dm^3 which is too high and may cause a laxative effect. The result indicates that the dye wastewater should not be released into the environment without treatment.

3.3. Photocatalytic behaviour of ZrO_2 based nanomaterials

The photocatalytic degradation of the local dyeing wastewater was examined using pure ZrO_2, ZrO_2 doped with 3wt% sulphur, ZrO_2 doped with 3wt% carbon and ZrO_2 co-doped with 3wt% carbon-sulphur under natural sunlight. The following physicochemical parameters (TOC, COD, BOD, SO_4^{2-}, CO_3^{2-}, Cl^-, NO_3^-, and pH) of the local dyeing wastewater were measured and the percentage reduction of each parameter was calculated and represented in Fig. 4.

The photocatalytic degradation in Fig. 4 revealed that the percentage removal of the indicator parameters increased with an increase in reaction time for all the samples. The percentage reduction of the COD, BOD, TOC, SO_4^{2-}, CO_3^{2-}, Cl^-, NO_3^- and pH compared with the original dyeing wastewater with respect to nanomaterial follow this order ZrO_2<ZrO_2-S<ZrO_2-C<ZrO_2-C-S with the carbon-sulphur co-doped ZrO_2 exhibited greater photocatalytic behaviour. The behaviour of the nanocatalyst can be linked to the differences in the band gap energy, morphology, crystallite size and surface area of the ZrO_2 based nanomaterial. For instance, ZrO_2 co-doped with carbon-sulphur has the least band gap (3.4 eV) and the highest surface area (80.165 m^2/g). This agrees with the findings of Davoodbeygi and Irankhah (2018) who investigated the photocatalytic properties of ZrO_2-ZnO nanoparticles synthesized by microwave irradiation method. The percentage removal of COD for carbon-sulphur co-doped ZrO_2 increased with increasing reaction time in the order 60.6% at 30 min < 65.3% at 60 min <67.8% at 90 min <77.3% at 120 min. BOD removal using carbon-sulphur co-doped ZrO_2 also follows the order: 77.5% at 30 min <80.3% at 60 min <82.6% at 90 min <87.6% at 120 min. Also, the percentage degradation of organic dyes expressed in the form of TOC for carbon-sulphur co-doped ZrO_2 was in the order of 70.1% at 30 min <71.4% at 60 min <73.4% at 90 min<97.7% at 120 min. The percentage removal of inorganic constituents (radical scavengers) such as SO_4^{2-} increased in the order 59.9% at 30 min<63% at 60 min<64.1% at 90 min<63.9% at 120 min. CO_3^{2-} removal was in order of 84.2% at 30 min<84.8% at 60 min>84.45 at 90 min>84.4% at 120 min. The percentage removal for Cl^- ion increased from 62.4% at 30 min to 67.6% at 60 min to 70.7% at 90 min and later decreased to 70.3% at 120 min. The percentage removal for NO_3^- increased from 78.1 % at 30 min to 83.9 % at 60 min to 84.7 % at 90 min and reduced to 83.3 % at 120 min.

It was also observed that the reaction time for the removal of each indicator parameter differs with respect to the nanocatalyst. For instance, the maximum removal efficiency of COD, BOD, TOC occurred at 120 min while the removal efficiency of the anions from the dyeing wastewater were 60 and 90 min for $CO_3^{2,}$ SO_4^{2-}, Cl^-, $NO_3^-$for carbon-sulphur co-doped ZrO_2 nanocatalyst. This implies the rate of removal of the pollutants depends on their mobility and competition with hydroxyl radicals for the active sites on the nanocatalyst. Thus, the catalytic efficiency of the four materials with respect to the removal of pollutants from dyeing wastewater was ZrO_2-S-C >ZrO_2-C>ZrO_2-S> ZrO_2. Hence ZrO_2-C-S composite has enhanced visible-light-driven activity.

Comparatively, carbon-doped ZrO_2 exhibited slightly higher catalytic activity than sulphur doped ZrO_2 nanomaterial due to the difference in band gap and the surface of the nanomaterial. The nanomaterial with a higher surface area has more active sites and tendencies to absorb visible light than material with a smaller surface area. The behavioural pattern of the nanocatalyst can also be linked to the phase-type. For instance, carbon-doped ZrO_2 nanoparticles exist in the monoclinic phase which is photocatalytically more active than the orthorhombic phase obtained for sulphur doped ZrO_2 nanoparticles (Fig. 2). Renuka et al., 2021)) synthesized Mg-doped ZrO_2 using *Aloe vera* extract for the degradation of Rhodamine Blue under UV light and found that pure

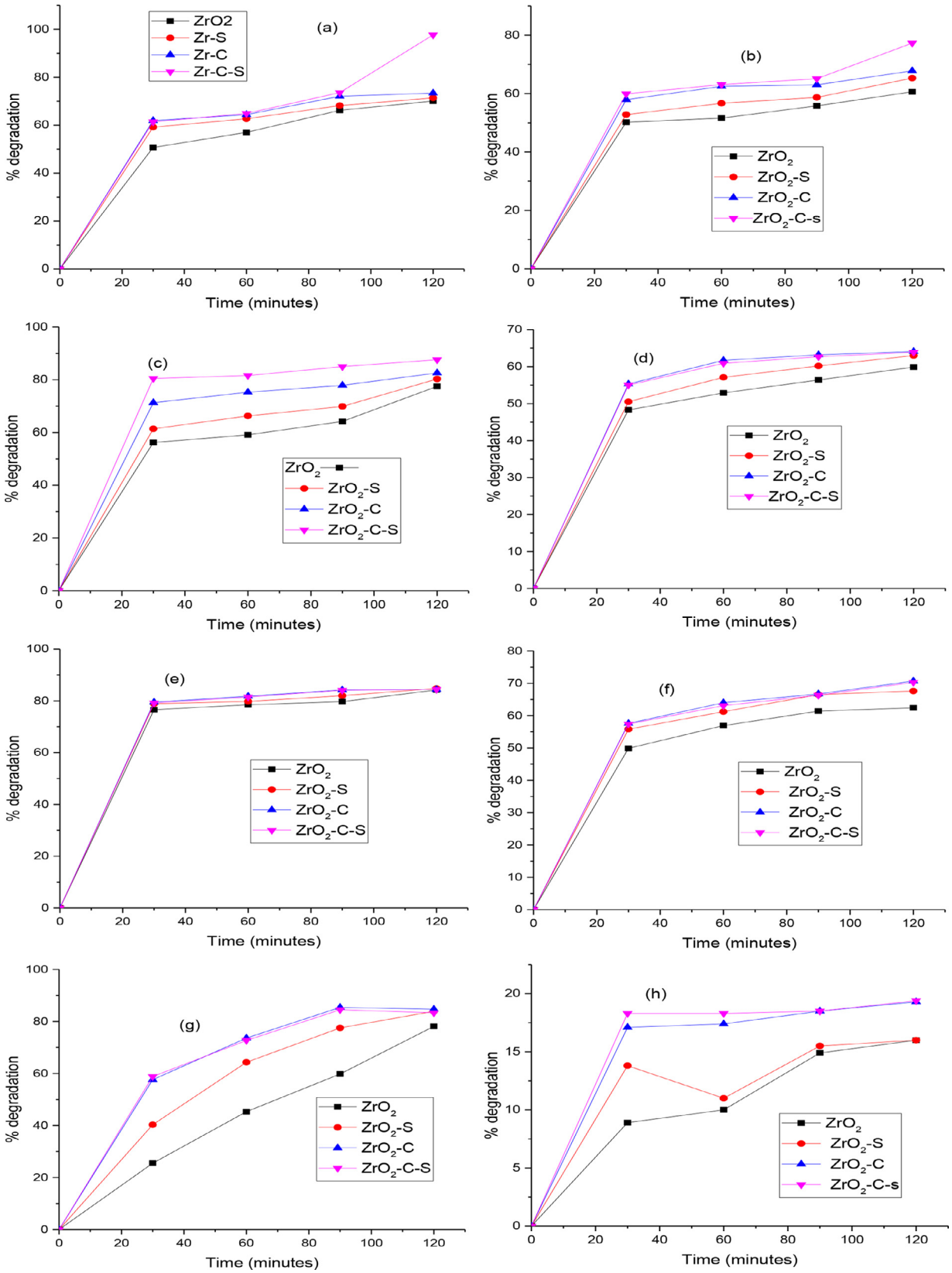

Fig. 4. Photocatalytic percentage removal efficiency of (a) TOC; (b) COD; (c) BOD; (d) SO_4^{2-}; (e) CO_3^{2}; (f) Cl^{-}; (g) NO_3^{-} and (h) pH by ZrO_2, ZrO_2 with 3% sulphur, ZrO_2 with 3% carbon and ZrO_2 with 3% carbon-sulphur.

Table 2
Physico-chemical properties of local dyeing wastewater before and after (a) Photocatalytic degradation and (b) Adsorption study with WHO (2017) and Nigerian industrial standards (NIS) (2007).

Parameters	Raw sample	Treatment				WHO	NIS
		Pure ZrO_2	ZrO_2-S	ZrO_2-C	ZrO_2-S-C		
(a)							
TOC	402	1.53	1.41	1.06	0.93	5	5
COD	1448	580.64	534.70	505.01	415.13	250	250
BOD	670	130.60	123.15	100.20	82.80	50	50
Sulphate	1634.90	735.40	639.04	610.30	590.02	100	100
Carbonate	3857.30	800.12	712.18	610.02	603.49	350-125	250
Chloride	4200	1790.40	1550.03	1414.30	1246.22	250	250
Nitrate	58.80	24.20	16.04	9.12	9.01	50	60
pH	8.7	7.11	7.11	7.09	7.01	6.5-8.5	6.5-8.5
(b)							
TOC	402	1.80	1.37	1.03	1.17	5	5
COD	1448	679.64	648.10	608.90	614.72	250	250
BOD	670	205.80	171.44	163.45	170.50	50	50
Sulphate	1634.90	680.86	630.59	602.14	616.45	100	100
Carbonate	3857.30	760.10	705.49	664.91	670.40	350-125	250
Chloride	4200	1704.69	1542.10	1402.57	1500.30	250	250
Nitrate	58.80	23.90	15.15	9.09	10.07	50	60
pH	8.7	7.89	7.70	7.20	7.14	6.5-8.5	6.5-8.5

ZrO_2 degraded 65% of the dye in 60 min and 93% degradation rate for Mg doped ZrO_2. This study records higher removal efficiency due to its higher surface area and lower band gap.

3.4. Adsorption behaviour of ZrO_2 based nanomaterials

The adsorption studies of the local dyeing wastewater were carried out using pure ZrO_2, ZrO_2 doped with 3wt% sulphur, ZrO_2 doped with 3wt% carbon and ZrO_2 co-doped with 3wt% carbon-sulphur in the darkness via the variation of reaction time from 0 to 120 min. The physico-chemical parameters (TOC, COD, BOD, SO_4^{2-}, CO_3^{2-}, Cl^-, NO_3^-, and pH) after the adsorption were measured and the percentage removal was calculated for each of the parameters and represented in Fig. 5.

The adsorption behaviour of the four samples in Fig. 5 revealed a percentage increase in the removal of indicator parameters as reaction time increases. The percentage removal of COD, BOD, TOC, SO_4-2-, CO_3^{2-}, Cl^-, NO_3^- and pH followed the order of ZrO_2<ZrO_2-S<ZrO_2-C<ZrO_2-C-S. The removal efficiency of the indicator parameters from local dyeing wastewater was ascribed to the surface area and porous nature of the nanomaterial. Carbon-sulphur co-doped ZrO_2 exhibits excellent adsorptive properties due to its high mesoporosity and surface area than others (Table 1). Zhang et al. (2020) also reported improved photocatalytic efficiency for gully-like double-sized mesoporous structural S-scheme g-C_3N_4/ZrO_2 composites with degradation efficiency of 53 to70% phenol after 150 min. The percentage adsorptive removal of COD for carbon-sulphur co-doped ZrO_2 increased with an increase in reaction time in the order of 53% at 30 min<55.2% at 60 min<57.9% at 90 min>57.5% at 120 min. The order of BOD removal for carbon-sulphur co-doped ZrO_2 is 69.3% at 30 min<74.4% at 60 min<75.6% at 90 min>74.6% at 120 min. Also, the percentage removal of TOC for carbon-sulphur co-doped ZrO_2 is in order of 55.2% at 30 min<65.9% at 60 min<74.4% at 90 min>70.9% at 120 min. The percentage removal of the SO_4^{2-} increased in the order 58.4% at 30 min<61.4% at 60 min<63.2% at 90 min>62.3% at 120 min. CO_3^{2-} increased in order of 80.3% at 30 min<81.7% at 60 min<82.7 at 90 min>82.6% at 120 min. The percentage removal for Cl^- increased from 59.4% at 30 min to 63.3% at 60 min to 66.6% at 90 min then reduced to 64.3% at 120 min. The percentage removal for NO_3^- increased from 59.4% at 30 min to 74.6 % at 60 min to 84.5% at 90 min and reduced to 82.9 at 120 min. Fig. 5 indicates that carbon-sulphur co-doped ZrO_2 behave differently with respect to the target pollutants; for instance, maximum COD, BOD, TOC, occurred within 120 min while maximum removal of CO_3^{2-}, SO_4^{2-}, Cl^-, NO_3^-, were 60 and 90 min. This difference may be linked to the competition for the binding site on the nanoadsorbents by the target pollutants. Table 2(a,b) show the photocatalytic and adsorptive behaviour of the four samples after treatment of local dyeing wastewater. The obtained values after treatment were compared with WHO and NIS standards.

Comparing the results in Table 2(a,b), it is obvious that all four samples have excellent photocatalytic and adsorption properties. However, 100% complete removals of the target pollutants were not achieved due to the high level of TDS and TSS which probably blocked the pores of the nanocatalyst and nanoadsorbent. This prevented proper interaction of the pollutants with the active or binding sites of the four materials. In addition, the concentration of sulphates and carbonates after treatment were above the permissible limits, this may be linked to the tendencies of inorganic anions such as SO_4^{2-} and CO_3^{2-} to inhibit the surface activity of photocatalyst by reducing the number of OH^- available on the photocatalyst surface. This can also be explained in terms of strong competition for the active sites between the hydroxyl radicals produced by ZrO_2 during the photocatalysis with the radical scavengers (SO_4^{2-}, NO_3^-, Cl^-, CO_3^{2-}) in the dyeing wastewater.

It can be observed from Table 3 that synthesised carbon-sulphur co-doped ZrO_2 nanocomposite in this study compared favourably with respect to percentage removal efficiency of the target pollutant (97.7%) than previously reported ZrO_2. This was attributed to the fact that carbon-sulphur co-doped ZrO_2 has the highest surface area (80.16 m^2/g), the lowest particle size of (12.40 nm) and the lowest band gap (3.4 eV). Complete removal of the target pollutants was not achieved due to the partial blockage of active sites on the catalyst/adsorbents by the suspended solids in the local dyeing wastewater. This prevents proper interaction of the catalyst/adsorbent with the adsorbate. The differences in the behaviour of the catalyst/adsorbent may also be linked to the method of synthesizing ZrO_2, experimental conditions, crystallite size, surface area and functional groups.

3.5. Photocatalytic kinetics of ZrO_2 based nanomaterials

Four different kinetic models namely zero-order; pseudo-first-order, parabolic model and the modified Freundlich model were used to describe the photodegradation of local dyeing wastewater under natural sunlight by the ZrO_2 based nanomaterials. The obtained results are represented in Table 4 and the order of fitness for the prepared nanomaterials to the kinetic models was ZrO_2/C/S> ZrO_2/S> ZrO_2/C> ZrO_2 for TOC, COD, BOD, SO_4^{2-}, CO_3^{2-}, Cl^- and NO_3^- in all the kinetic models used.

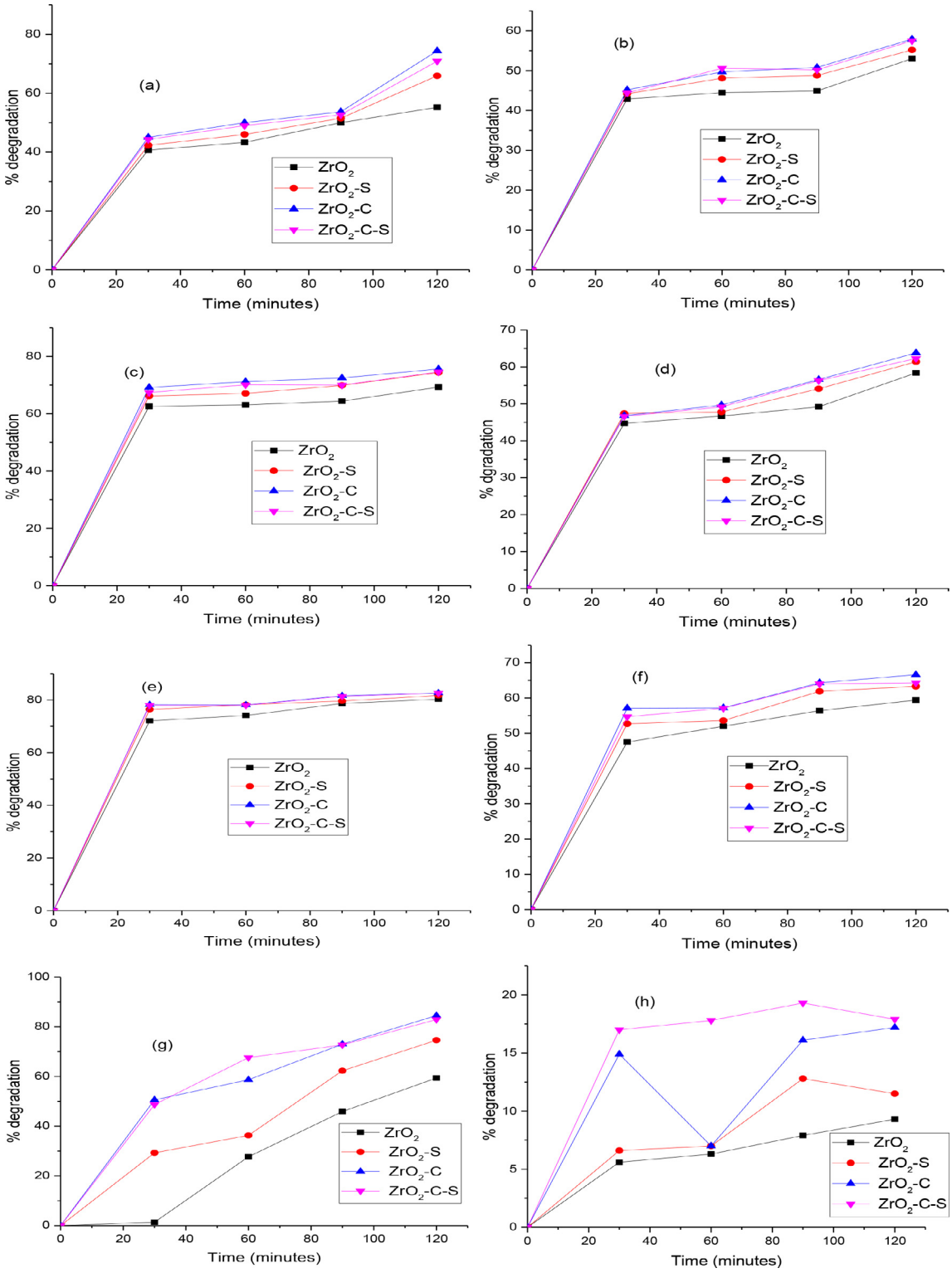

Fig. 5. Adsorptive percentage removal efficiency of (a) TOC; (b) COD; (c) BOD; (d) SO_4^{2-}; (e) CO_3^{2-}; (f) Cl^-; (g) NO_3^- and (h) pH by ZrO_2, ZrO_2 with 3% sulphur, ZrO_2 with 3% carbon and ZrO_2 with 3% carbon-sulphur.

The difference in photocatalytic performance may be due to the decrease in band gap and increase in surface area of the ZrO_2 nanomaterial from the mono-doped to the co-doped (Danilenko et al., 2018). Based on the correlation coefficient (R^2), the parabolic model best fitted for the TOC and NO_3^-. This is because the correlation coefficient (R^2) is closer to unity in the parabolic model for TOC and NO_3^-. This signifies that the degradation of organic dye is based on the reactive species (OH^- and O_2). The order of fitness in terms of correlation coefficient (R^2) for TOC removal is a parabolic model (0.9805) > pseudo first order (0.9711) > zero order (0.9703) > modified Freundlich model (0.9642). For COD reduction, the order of fitness are parabolic model (0.9984)>modified Freundlich model (0.9934) > pseudo first order (0.9912)>zero order

Table 3
Comparison of photocatalytic/adsorptive performance of previous synthesized ZrO_2 based nanomaterial with present study.

Authors	Synthesis method	Nano catalyst	Particle size				
(nm)	Band gap (eV)	Surface area (m^2/g)	% Degradation in Time (mins)	Type of			
Dye							
Kadi and Mohamed (2013)	Sol-Gel/ Photo-assisted deposition	ZrO_2-SiO_2/Pt	13.3	2.48	-	100 in 20	Cyanide
Agorku et al. (2015)	Co-precipitation	C,N,S-doped ZrO_2,					
	8–30	3.01	-	54.1 in 130	Indigo carmine		
Rani et al. (2016)	Combustion	GR- ZrO_2	33.9	3.32	45	88 in 120	Methylene blue
Wang et al. (2018)	Sol-gel	N-ZrO_2	20.3	4.00	217	87 in 90	Methylene orange
Park and Shao (2019)	Sol-gel	Ze- ZrO_2	40.80	5.6	76.31	90.5 in 120	Methyl orange
Dawoud et al. (2020)	Combustion	Ag- ZrO_2	10-16	5.6	30.4	95 in 105	Rhodamine B
Długosz et al. (2019)	Microwave irradiation	ZrO_2- ZnO	-	3.17	-	97 in 30	Methylene Blue
Ahmed et al. (2021)	Combustion	Ag- ZrO_2	16	5.6	30.406	75 in 120	Rhodamine blue
Uribe López et al. (2019)	Sol-gel	ZnO-ZrO_2	18.2	3.75	8.00	50 in 120	Indigo red
Nova et al. (2021)	Hydrothermal	Ag@ZrO_2	40-50	5.29	-	98 in 60	Rhodamine B
Haq et al. (2021)	Green	ZnO-ZrO_2	70	3.81	153.85	97.30 in 60	Rhodamine 6G
Al-Zaqri et al. (2021)							
Biosynthesis	ZrO_2	9.2	3.78	-	94.00 in 120	RY 160	
This study	Green	C-S-ZrO_2	12.4	2.6eV	80.16	97.7% in 120	Azo

Table 4
Kinetic models of photocatalytic behaviour of ZrO_2, S-ZrO_2, C-ZrO_2 and C-S-ZrO_2 nanomaterials.

Pollutant	Sample	Zero-order		First-order		Parabolic			Modified Freundlich	
		K	R^2	K	R^2	A	k	R^2	K	R^2
TOC	ZrO_2	0.0030	0.7921	0.0020	0.8099	0.0397	0.0002	0.8606	0.0118	0.8659
	ZrO_2/S	0.0034	0.8202	0.0022	0.8351	0.5758	0.0059	0.9558	0.0144	0.8893
	ZrO_2/C	0.0035	0.9503	0.0028	0.9344	0.8539	0.0098	0.9629	0.0149	0.9004
	ZrO_2/C/S	0.0048	0.9703	0.0029	0.9711	1.1358	0.0158	0.9805	0.0162	0.9642
COD	ZrO_2	1.6526	0.9233	0.0025	0.9285	0.0010	1 × 10-5	0.8402	0.0107	0.9552
	ZrO_2/S	1.6705	0.9743	0.0028	0.9752	0.0012	2 × 10-5	0.9572	0.0144	0.9685
	ZrO_2/C	1.7712	0.9841	0.0031	0.9859	0.0015	3 × 10-5	0.9745	0.0177	0.9821
	ZrO_2/C/S	1.9370	0.9857	0.0034	0.9912	0.0017	4 × 10-5	0.9954	0.0244	0.9934
BOD	ZrO_2	0.7271	0.9679	0.0091	0.9332	0.0108	0.0002	0.6714	0.0175	0.9355
	ZrO_2/S	1.5873	0.9839	0.0094	0.9552	0.0125	0.0003	0.8505	0.0383	0.9516
	ZrO_2/C	1.7127	0.9959	0.0098	0.9732	0.0162	0.0004	0.8814	0.0418	0.9762
	ZrO_2/S/C	1.8478	0.9960	0.0099	0.9907	0.0183	0.0006	0.8824	0.0449	0.9896
Sulphate	ZrO_2	1.2032	0.8890	0.0018	0.8145	0.0010	1×10^{-5}	0.8601	0.0142	0.8785
	ZrO_2/S	1.4069	0.9159	0.0024	0.9131	0.0014	2×10^{-5}	0.8899	0.0169	0.9295
	ZrO_2/C	1.6498	0.9323	0.0028	0.9151	0.0017	3×10^{-5}	0.9431	0.0177	0.9525
	ZrO_2/S/C	1.7367	0.9369	0.0031	0.9401	0.0019	4×10^{-5}	0.9449	0.0277	0.9681
Carbonate	ZrO_2	5.5004	0.5007	0.0014	0.7799	0.0036	0.0001	0.8992	0.0010	0.8458
	ZrO_2/S	5.9813	0.8768	0.0020	0.9123	0.0038	2×10^{-4}	0.9335	0.0052	0.8831
	ZrO_2/C	6.9547	0.9007	0.0030	0.9250	0.0061	3×10^{-4}	0.9335	0.0065	0.9473
	ZrO_2/S/C	7.7065	0.9577	0.0040	0.9381	0.0242	4×10^{-4}	0.9578	0.0090	0.9592
Chloride	ZrO_2	2.1613	0.6347	0.0014	0.6372	0.0006	0.0002	0.8011	0.0091	0.7228
	ZrO_2/S	3.2516	0.8631	0.0018	0.7855	0.0008	4×10^{-4}	0.8543	0.0131	0.8516
	ZrO_2/C	3.4315	0.9023	0.0020	0.8782	0.0009	5×10^{-4}	0.9006	0.0141	0.9232
	ZrO_2/S/C	3.8707	0.9750	0.0028	0.9154	0.0381	8×10^{-4}	0.9327	0.0157	0.9529
Nitrate	ZrO_2	0.0030	0.7921	0.0022	0.8099	0.0397	0.0002	0.8606	0.0118	0.8659
	ZrO_2/S	0.0034	0.8202	0.0025	0.8351	0.5758	0.0059	0.9558	0.0144	0.8893
	ZrO_2/C	0.0035	0.9503	0.0028	0.9344	0.8539	0.0098	0.9629	0.0146	0.9004
	ZrO_2/S/C	0.0048	0.9703	0.0029	0.9711	1.1358	0.0158	0.9805	0.0205	0.9642

(0.9857). For the removal of NO_3^-, the order of fitness are: parabolic model (0.9805)> pseudo first order (0.9711) > zero order (0.9703) > modified Freundlich model (0.9642). The zero-order kinetics best fitted for BOD and Cl^-. This signifies that the photocatalytic degradation of the azo dyes in wastewater did not depend on the concentration of the pollutants. The order of BOD removal is: zero-order (0.996) >pseudo first order (0.9907) > modified Freundlich model (0.9896) > parabolic model (0.9824). The modified Freundlich model was best fitted for SO_4^{2-} and CO_3^{2-} removal which suggest that the catalytic degradation of organic dyes occurred on the catalyst surface before desorption in the aqueous medium and the reaction followed homogenous diffusion and adsorption-desorption mechanism. Agarwal et al. (2016) reported the fitness of kinetic data to modified Freundlich and Langmuir model polyaniline/ZrO_2 nanocomposites used to degrade anyline photocatalytically.

3.6. Adsorption kinetics of ZrO_2 based nanomaterials

The adsorption studies of the organic dyes from dyeing wastewater was carried out in the dark and there was a corresponding decrease in the TOC, COD, BOD, SO_4^{2-}, CO_3^{2-}, Cl^-, NO_3^- and pH values using the synthesized pure ZrO_2, ZrO_2-sulphur, ZrO_2-carbon and carbon-sulphur-ZrO_2. Four different kinetic models (zero-order, pseudo-first-

Table 5
Kinetic model of adsorptive behaviour of ZrO_2, S-ZrO_2, C-ZrO_2 and C-S-ZrO_2 nanomaterials.

Pollutant	Sample	Zero-order		First-order		Parabolic			Modified Freundlich	
		K	R^2	K	R^2	A	k	R^2	K	R^2
TOC	ZrO_2	0.0018	0.7857	0.0013	0.7814	0.0375	0.0029	0.7305	0.0019	0.8135
	ZrO_2/S	0.0028	0.8050	0.0015	0.7999	0.1982	0.0231	0.8284	0.0034	0.8293
	ZrO_2/C	0.0054	0.8100	0.0017	0.8038	0.3190	0.0235	0.8818	0.0060	0.8600
	ZrO_2/S/C	0.0074	0.8368	0.0053	0.8170	0.4281	0.1474	0.8944	0.0319	0.8703
COD	ZrO_2	0.2740	0.5464	0.0003	0.5430	0.0006	0.0003	0.9369	0.0033	0.6340
	ZrO_2/S	0.7444	0.6121	0.0012	0.6203	0.0007	6×10^{-4}	0.9487	0.0121	0.9597
	ZrO_2/C	0.8664	0.7584	0.0017	0.7610	0.0009	8×10^{-4}	0.9507	0.0140	0.9650
	ZrO_2/S/C	0.9799	0.8488	0.0022	0.8475	0.0012	9×10^{-4}	0.9811	0.0191	0.9951
BOD	ZrO_2	0.3888	0.6471	0.0017	0.6360	0.0009	0.0069	0.7602	0.0043	0.7506
	ZrO_2/S	0.4614	0.7967	0.0026	0.7708	0.0026	0.0078	0.7794	0.0101	0.7682
	ZrO_2/C	0.5286	0.8522	0.0027	0.8892	0.0029	0.0089	0.7851	0.0114	0.8195
	ZrO_2/S/C	0.6796	0.8925	0.0029	0.8952	0.0050	0.0096	0.7916	0.0126	0.8932
Sulphate	ZrO_2	0.2783	0.5985	0.0003	0.6271	0.0006	0.0001	0.7503	0.0010	0.6202
	ZrO_2/S	0.5109	0.7966	0.0006	07936	0.0008	3×10^{-4}	0.8351	0.0053	0.8391
	ZrO_2/C	1.6019	0.8128	0.0017	0.8197	0.0012	6×10^{-4}	0.8922	0.0136	0.8823
	ZrO_2/S/C	0.9389	0.8977	0.0019	0.8962	0.0015	0.0009	0.9025	0.0179	0.8855
Carbonate	ZrO_2	1.2938	0.7826	0.0016	0.5573	0.0011	0.0003	0.7712	0.0065	0.6529
	ZrO_2/S	1.4740	0.8008	0.0026	0.7939	0.0014	0.0006	0.7968	0.0111	0.8580
	ZrO_2/C	1.5284	0.8688	0.0057	0.8647	0.0023	0.0008	0.9009	0.0157	0.8879
	ZrO_2/S/C	1.7323	0.8740	0.0075	0.8771	0.0031	0.0009	0.9012	0.0246	0.8955
Chloride	ZrO_2	1.6675	0.6805	0.0012	0.6704	0.0055	0.0036	0.7683	0.0251	0.7588
	ZrO_2/S	2.6565	0.7740	0.0014	0.7711	0.0083	0.0058	0.8318	0.0305	0.8329
	ZrO_2/C	3.5513	0.7939	0.0021	0.8030	0.0113	3×10^{-4}	0.9101	0.0345	0.8673
	ZrO_2/S/C	4.5090	0.7956	0.0026	0.8806	0.0124	5×10^{-4}	0.9459	0.0405	0.8780
Nitrate	ZrO_2	0.2421	0.8700	0.0063	0.8594	0.0009	0.0008	0.7015	0.0691	0.9072
	ZrO_2/S	0.2783	0.9641	0.0095	0.9622	0.0025	0.0017	0.7933	0.0771	0.9484
	ZrO_2/C	0.2800	09164	0.0181	0.9651	0.0174	0.0234	0.8409	0.0891	0.9672
	ZrO_2/S/C	0.3585	0.9212	0.0193	0.9777	0.0258	0.0553	0.8629	0.0960	0.9860

order, parabolic model and the modified Freundlich model) were used to describe the adsorption data and the obtained result is presented in Table 5.

From Table 5, the order of fitness of the prepared ZrO_2 nanomaterials for TOC was ZrO_2<ZrO_2-sulphur<ZrO_2-carbon<ZrO_2-carbon-sulphur for all the kinetic models. This may be attributed to the increase in surface area and increased mesoporosity as a function of doping and co-doping. The modified Freundlich model was the best fit with (0.8103)>zero order (0.7368)> parabolic model (0.7344) for TOC removal. For COD removal, the fitness to the model based on the correlation coefficient (R^2) is Freundlich (0.9597) > parabolic (0.9487) > pseudo-first-order (0.9203) > zero-order (0.9121) with ZrO_2-sulphur as best suited nanomaterial. The fitness of the Freundlich model indicates a homogenous diffusion and the occurrence of the degradation of organic dyes on the photocatalyst surface. For BOD removal, zero-order is best fitted with R^2 value (0.7967) > parabolic model (0.7794) > pseudo first order (0.7708) > modified Freundlich model (0.7282) with ZrO_2-S best-suited nanomaterial. For SO_4^{2-} removal, the parabolic model is best fitted with R^2 value (0.8922) > modified Freundlich model (0.8823) > pseudo first order (0.8197)>zero order (0.8128) with ZrO_2-C nanomaterial having the highest correlation. In the case of CO_3^{2-} removal, the fitness of the data followed this order parabolic model (0.9012)>modified Freundlich model (0.8955)>zero order (0.8688)>pseudo first order (0.8647) with ZrO_2-carbon best-fitted nanomaterial. For the Cl^-, the parabolic model was best fitted with (0.9101)>zero order (0,8744)>pseudo first order (0.8711)>modified Freundlich model (0.8673) with ZrO_2-carbon as best fitted nanomaterial. The fitness of the parabolic model for sulphate, carbonate and chloride signifies the degradation of organic dyes through the reactive species (OH^- and O_2) was based on the diffusion mechanism. While for the NO_3^-, the zero-order was best fitted with (0.9644)> pseudo-first-order (0.9622)>modified Freundlich model (0.9484)>parabolic model (0.9409) with ZrO_2-C having the highest correlation efficiency (R^2). Tsegaye et al. (2020) found that the modified Freundlich model best fitted for the removal efficiency of cadmium and chromium ion by Fe-Al co-doped ZrO_2 nanocomposite. Comparatively, the maximum adsorptive capacity reported in this study is significantly higher than others presented in Table 6 despite higher concentration of the adsorbate in the real wastewater and short reaction time This behaviour may be due to the co-doping effects of carbon and sulphur on ZrO_2 nanoparticles which enhanced to its surface area and adsorptive efficiency. Fig. 3 and Table 1 respectively.

3.7. Mechanism of ZrO_2 based nanomaterial

The photocatalytic mechanism can be explained based on the adsorption, diffusion and complexation of the molecules of dye on the surface of the ZrO_2 based nanomaterial. However, the photocatalytic efficiency of ZrO_2 is limited by the quick recombination of excited electron-hole pairs and the large band gaps (5.2 eV). As a result, the co-doping effect of carbon and sulphur improved the photo-response of ZrO_2 to visible light by narrowing the band gap (3.4 eV) and lowering the high charger carrier recombination rate (Fig. 3I and II) (Guo et al., 2020). The reduction in the band gap energy due to carbon and sulphur impurities contributed to the improved catalytic activity of ZrO_2. Therefore, the generation of reactive species occurred upon the interaction of C-S-ZrO_2 with visible light caused electrons excitation from the conduction band to valence band and generation of electron-holes pairs as shown in Fig. 6a.

It was noticed from the PL result that the addition of carbon and sulphur reduced the intensity of ZrO_2, evidence of suppression of electron-holes pairs. This means that the photogenerated electrons from carbon reach ZrO_2 via sulphur and vice-versa. The reaction scheme during the photodegradation of azo dyes in local dyeing wastewater by C-S-ZrO_2 under sunlight irradiation is shown in Eqs. (5)–(9).

$$\text{Catalyst}\left(C - S - ZrO_2\right) + hv \rightarrow C - S - ZrO_2\left(h^+ + e^-\right) \quad (5)$$

$$e^- + O_2 \rightarrow O_2^- \quad (6)$$

$$h^+ + H_2O \rightarrow OH + H^+ \quad (7)$$

Table 6
Comparison of maximum adsorption capacity of C-S-ZrO_2 composite with previous nanoadsorbent reported in literature.

S/N	Adsorbents	Adsorbate	Experimental conditionsConc. (mg/L)	pH	Temp(K)	Time (h)	dosage (g)	Maximum adsorption capacity(q_{max}) (mg/g)	Refs.
1	ZrO_2	Phosphate	5	6.2	298	4	0.1	99.01	Su et al. (2013)
2	ZrO_2	Methylene blue and rhodamine B	4	10, 11	298	1	0.5	9.98	Rani et al., (2016)
3	Fe_3O_4/ZrO_2	Phosphate	2	7.6	298	0.166	0.6	15.55	Wang et al. (2017)
4	Fe_3O_4/ZrO_2	Phosphate	50	4	298	24	2.0	13.99	Zhang et al. (2017)
5	ZrO_2	Lead (Pb)	100	3	298	5	1	104.4	Wei et al. (2018)
6	ZrO_2	Methyl orange	22	8.0	298	0.42	0.54	370.37	Bhowmik et al. (2018).
7	Fe_3O_4/ZrO_2	Lead (Pb)	20	7	298	6	0.5	108	Irawan et al. (2022)
8	ZrO_2	Methylene blue	20	10	298	6	0.3	23.26	Alagarsamy et al. (2022)
9	C-S-ZrO_2	Azo dye	402	8.7	298	2	0.5	422.4	This study

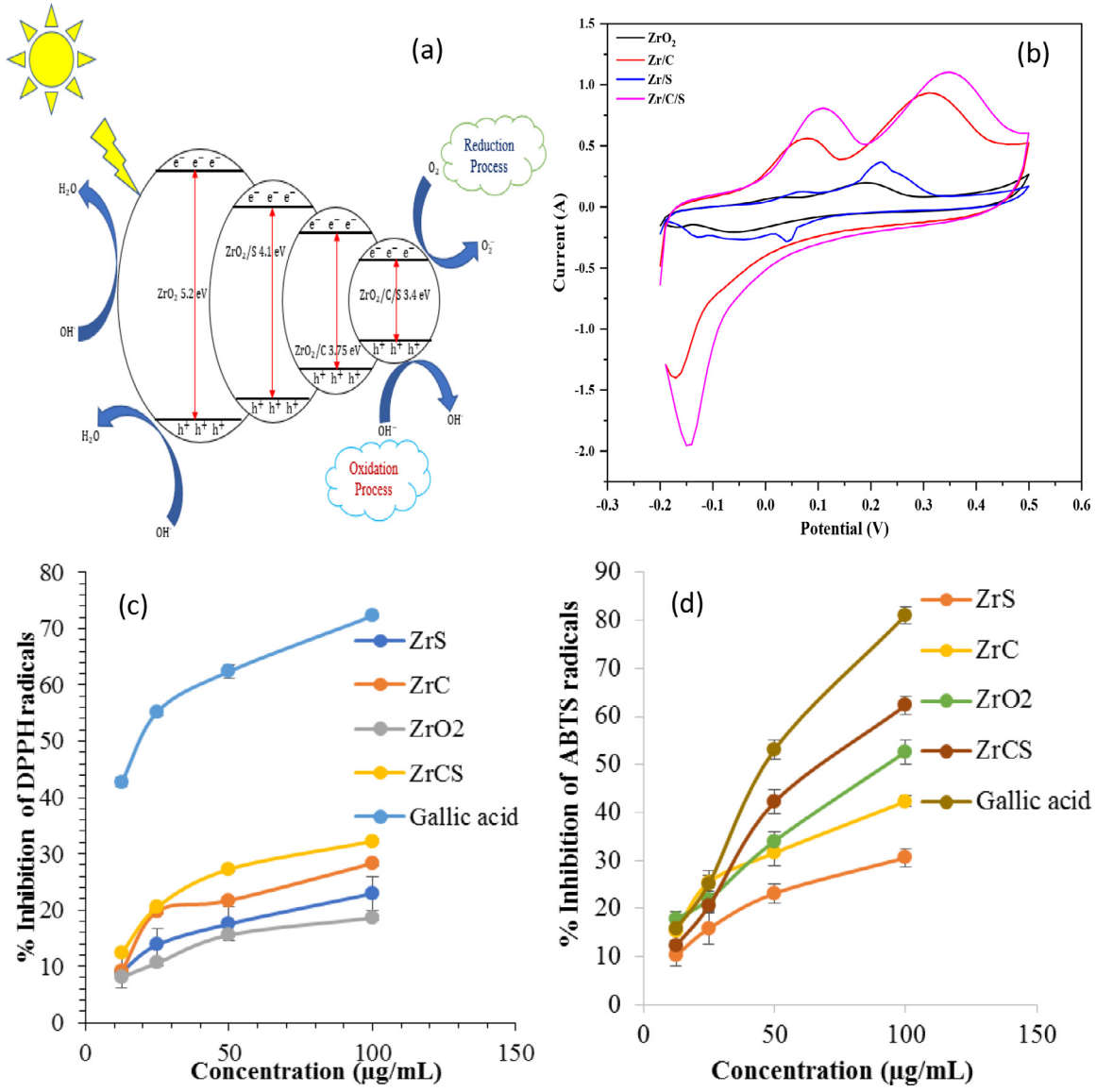

Fig. 6. (a) Schematic representation of photocatalytic mechanism of ZrO_2 based nanomaterial; (b) Cyclic voltammetry curves of ZrO_2, Zr/C, Zr/S and Zr/C/S at 50 mV/s in 0.2 M H_2SO_4, Ag/AgCl as reference electrode; (c) DPHH Antioxidant activity of zirconium oxide nanoparticles and their composite and (d) ABTS Antioxidant activity of zirconium oxide nanoparticles and their composite.

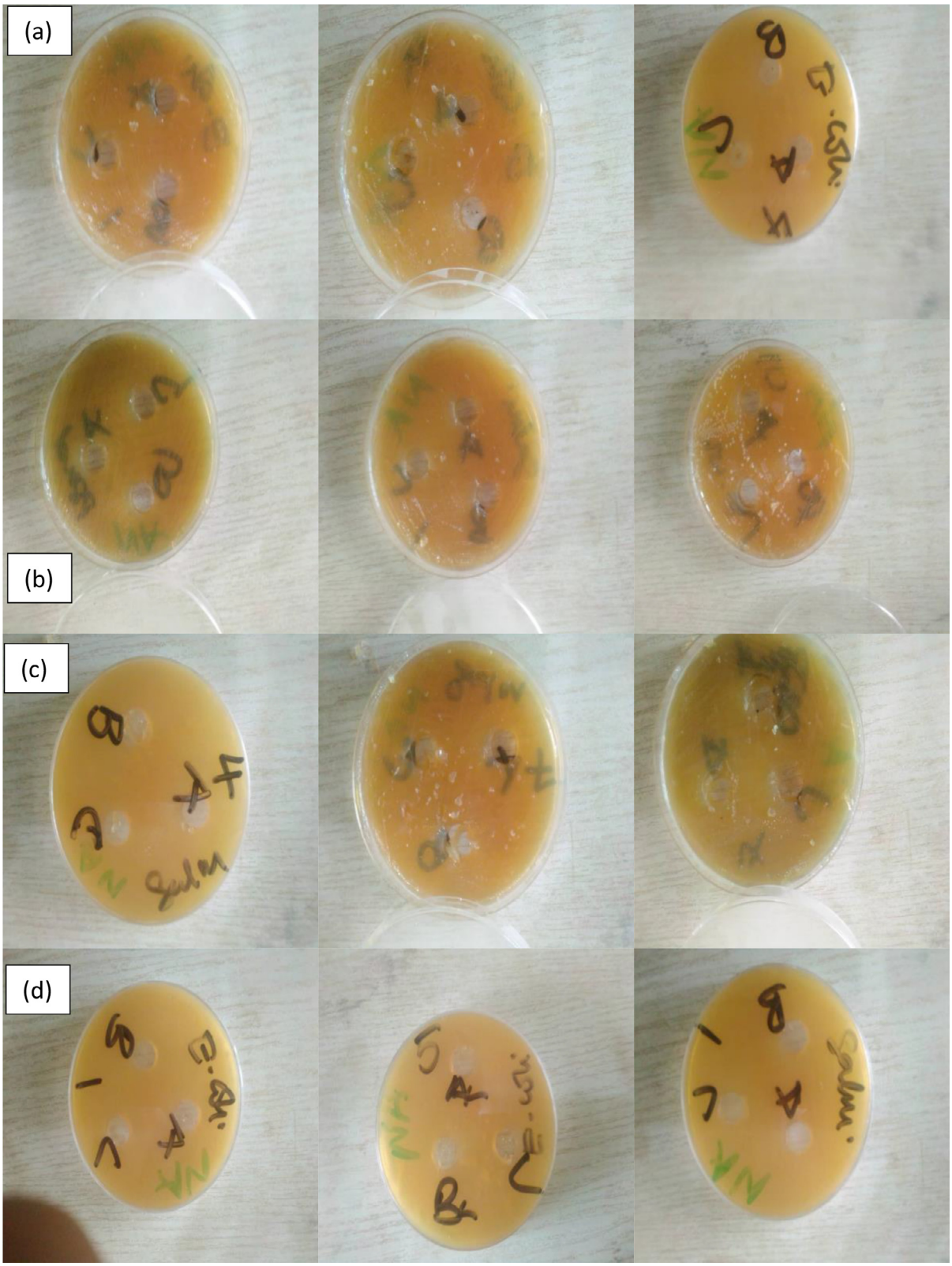

Fig. 7. Marked zone of Inhibition of the prepared (a) ZrO_2 alone (b) ZrO_2 with 3% sulphur (c) ZrO_2 with 3% carbon (d) ZrO_2 with 3% carbon-sulphur against E. coli, P. aeruginosa and S. typhi.

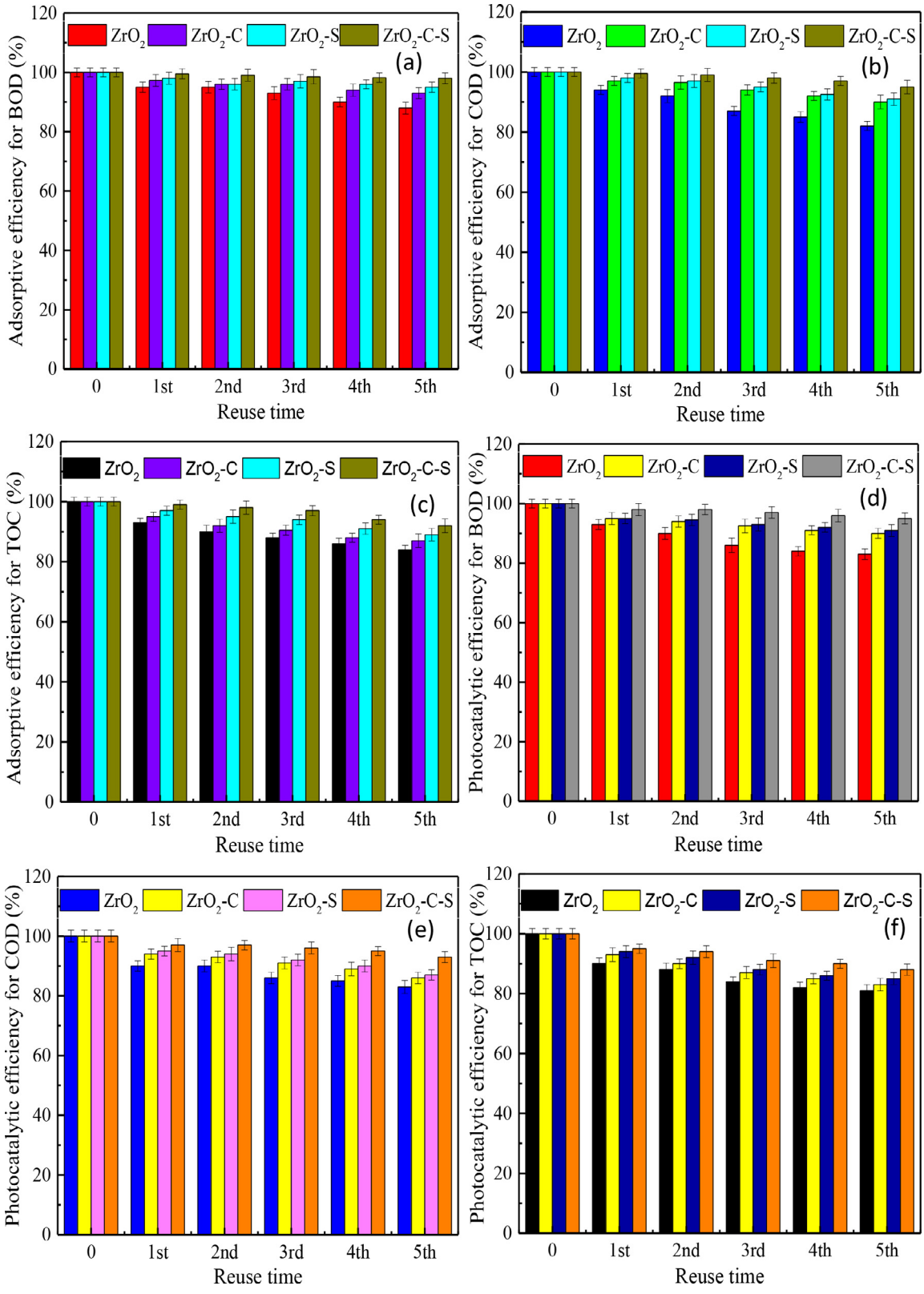

Fig. 8. Reusability investigation of the adsorptive efficiency of zirconium oxide nanoparticles and its composites towards (a) BOD; (b) COD; (c) TOC; photocatalytic degradation efficiency of the zirconium oxide nanoparticles and its composites towards (d) BOD; (e) COD and (f) TOC.

$$\mathbf{OH^- + Organic\ Pollutants \rightarrow Decomposition\ products}\left(\mathbf{CO_2 + H_2O}\right) \quad (8)$$

$$O_2^- + \text{Organic Pollutants} \rightarrow \text{Decomposition products}\left(CO_2 + H_2O\right) \quad (9)$$

The superoxide radical anion (O_2^-) is formed when electrons in the conduction band of C-S/ZrO_2 interact with adsorbed oxygen molecules in the medium (Xu et al., 2020). Photo-induced holes with a high oxidizing power react with hydroxyl groups on the catalyst (C-S/ZrO_2) surface to create the highly reactive (·OH) radical (Ahmad et al., 2020). These superoxide radicals (O_2^-) and highly reactive (·OH) species react with adsorbed contaminants on the catalyst surface, causing it to deteriorate and yield degradation products (Bommalapura and Al-Gunaid, 2021). The photocatalytic reaction of C-S/ZrO_2 was faster than others due to its enhanced mesoporosity (more active sites) and higher surface area. These highly reactive species (•O_2^-, HO_2. and •OH) contributed to the decomposition of azo dye related compounds. Also, •OH species in the medium react with H^+ ions and formed hydrogen peroxide (H_2O_2) that reacts further with electrons from C-S-ZrO_2, to enhance the concentration of hydroxyl radicals in the medium and eventually enhance the degradation process of dyes into carbon (IV) oxide and water respectively.

3.8. Electrochemical behaviour

The electrochemical studies of the ZrO_2, S-ZrO_2, C-ZrO_2, and C-S-ZrO_2 are evaluated using Cyclic Voltammetry (CV) over the potential range from -0.2 to 0.5 V at a scan rate of 50 mV/s and the result is depicted in Fig. 6b. This result reveals the cathodic peak potential at -0.06 and -0.17 V for ZrO_2, -0.17 for ZrO_2/C, -0.13 and 0.04 V for ZrO_2/S and -0.15 V for ZrO_2/S/C. The anodic waves are 0.03 and 0.19 V for ZrO_2, 0.08 and 0.32 V for ZrO_2/C, 0.08 and 0.22 V for ZrO_2/S, and 0.11 and 1.12 V for ZrO_2/S/C. During the doping processes, the cathodic and anodic rate increase could be associated with the complete diffusion of the dopants onto zirconium. The disappearance of the cathodic peak of S in Zr/C/S may be due to the carbon effect. More so, the peak current of C-S-ZrO_2 increases due to its highest surface area and this may be as a result of the passivation phenomenon associated with the dopants. The carbon and sulphur dopant increases the intercalation rate and the rearrangement of the lattice layer of ZrO_2. It is noteworthy that the potential peaks shift to more positive values for ZrO_2/C (0.32 V), ZrO_2/S (0.22 V) and ZrO_2/S/C (1.12 V) compared to ZrO_2 (0.19 V) and the oxidation processes shifted to more positive values. This shows that the reduction process was more in the doped ZrO_2 nanoparticles and the interactions of carbon and sulphur with the oxygen sites was very strong.

3.9. Antioxidant activity

Fig. 6d represents the antioxidant activity of the ZrO_2 nanoparticles and its composites. It was noticed that increase in the concentration of the ZrO_2 based nanomaterial (antioxidant) corresponds to a percentage increase in the inhibitory effect or free radical scavenging activity. The increment was found to be concentration-dependent due to the larger number of antioxidants present in the solution, which can counter a larger number of ABTS free radicals The DPPH radical scavenging assay shows a moderate level of antioxidant activity with IC_{50} ranging between 177.60 and 359.46 μg/mL compared with Gallic acid (standard) with an IC_{50} of 19.99 μg/mL (Fig. 6c) while the ABTS assay has an IC_{50} ranging between 74.22 and 181.78 μg/mL and compared with Ascorbic acid (standard) with an IC_{50} of 55.09 μg/mL (Fig. 6d). The observed antioxidant activity exhibited by the nanoparticles and its composites may be attributed to their hydroxyl groups which are present in the nanoparticles similar to the phenolic functional group. The IC_{50} value is a parameter widely used to measure the antioxidant activity of test samples. It is the concentration of antioxidants needed to inhibit 50% of DPPH or ABTS radicals (Rivero-Cruz et al., 2020). Hence, the lower the IC_{50} value the higher the antioxidant activity. Antioxidant activity of compounds have been classified based on their IC_{50} as a high (IC_{50} < 1 μM), a moderate (1 μM < IC_{50} < 10 μM), and a low (IC_{50} > 10 μM) (Keshavarz-Shokri et al., 2018). Based on these classifications, the nanoparticles and its composite exhibit a moderate antioxidant activity with Zr-C-S ranking higher in both DPPH and ABTS assay than other ZrO_2 based nanomaterials due to its higher surface area and more active binding sites than others.

3.10. Antibacterial behaviour

The antibacterial behaviour of the synthesised ZrO_2 nanoparticles and its composites prepared at a concentration (400 mg/mL) against Gram-positive (*Salmonella typhi* and *Pseudomonas aeruginosa*) and Gram-negative bacteria (*Escherichia coli*) with zones of inhibition ranging between 6.33±0.90 and 25.10±1.80 mm with *P. aeruginosa* most susceptible are presented in (Table S2).

The order of antibacterial activity of the nanomaterials against the selected bacteria is C-S-ZrO_2> C-ZrO_2> S-ZrO_2>ZrO_2. The antibacterial action of the nanoparticles and its composite may be attributed to their ability to penetrate the bacterial membrane and inhibit the functional properties of the cell as evident in the crystallite size of the nanoparticles (Buszewski et al., 2019). The antibacterial activity may also be attributed to the hydrophobicity of these materials which allows them to separate the lipids from the cell membrane and cause an increase in cell permeability (Hardin et al., 2009). Compounds rich in hydroxyl groups can alter the permeability of the microbial cell, damage the cytoplasmic membrane, interfere with the cellular energy generation system (ATP), and disrupt the proton motive force, leading to cell death (Buszewski et al., 2019). The enhanced destruction of the bacteria cells strongly suggests C-S-ZrO_2 as excellent antibacterial material than others due to its large surface area, spherical shapes with small particle size. This result shows that the carbon-sulphur synergistic effects, as well as its high surface energy, may be responsible for the efficient antibacterial behaviour of C-S-ZrO_2

3.11. Regeneration studies

The ability of the zirconium oxide nanoparticles and its composites to be recycled and reused is of important concern to ascertain their potential suitability for practical adsorption and photocatalytic applications in real wastewater treatment system. Therefore, the desorption analysis of the exhausted ZrO_2, C-ZrO_2, S-ZrO_2 and C-S-ZrO_2 was examined for the removal of BOD, COD and TOC as shown in Fig. 8(a–f).

According to Fig. 8(a–c), the zirconium oxide nanoparticles and its composites were successfully regenerated and reused for five consecutive cycles with the removal capacity of BOD (88, 93, 95 and 98% for ZrO_2, C-ZrO_2, S-ZrO_2 and C-S-ZrO_2), COD (82, 90, 91 and 95% for ZrO_2, C-ZrO_2, S-ZrO_2 and C-S-ZrO_2) and TOC (84, 87, 89 and 92% for ZrO_2, C-ZrO_2, S-ZrO_2 and C-S-ZrO_2), respectively. Also, Fig. 8(d–f) the degradation capacity of the photocatalytic process was obtained for BOD (83, 90, 91 and 95% for ZrO_2, C-ZrO_2, S-ZrO_2 and C-S-ZrO_2), COD (83, 86, 87 and 93% for ZrO_2, C-ZrO_2, S-ZrO_2 and C-S-ZrO_2) and TOC (81, 83, 85 and 88% for ZrO_2, C-ZrO_2, S-ZrO_2 and C-S-ZrO_2) after the fifth cycle. The trend of the zirconium oxide nanoparticles and its composite reusability results indicate satisfactory evidence to be recovered and reused in the treatment of dyeing wastewater using both adsorption and photocatalytic methods.

4. Conclusion

The synthesis of ZrO_2 based nanoparticles was carried out using the green method. The zirconium oxide doped nanomaterials were prepared characterized. The prepared ZrO_2 nanomaterials were utilized as nanocatalyst and nano-adsorbent to treat local dyeing wastewater. The electrochemical, antibacterial and antioxidant behaviour of a novel

carbon-sulphur co-doped zirconium oxide was investigated. Based on these, the following conclusion was drawn; HRSEM, XRD, BET, HRTEM, UV-visible spectrometer, SAED and EDS confirmed successful incorporation of carbon and sulphur into the lattice layer of ZrO_2 as evidence in the reduction of band gap from 5.2 eV to 3.4 eV. The incorporation of carbon and sulphur onto the lattice layer of ZrO_2 enhanced the surface area in the order of sulphur-ZrO_2 (24.824 m^2/g) <carbon-ZrO_2 (52.637 m^2/g)<carbon-sulphur-ZrO_2 (80.165 m^2/g) compared to ZrO_2 alone with a surface area of 10.68 m^2/g. The order of photocatalytic/adsorptive/electrochemical/antibacterial/antioxidant performance of the four nanomaterials were carbon-sulphur co-doped ZrO_2> carbon-doped ZrO_2> sulphur- doped ZrO_2 > ZrO_2 in the presence and absence of natural sunlight. The enhanced multi-functional behaviour of ZrO_2-C-S can be linked to their morphology, phase-type, crystallite size, porosity and surface area. The study demonstrated that C-S-ZrO_2 nanocomposite has reusable for repeated applications even after five cycles.

Declaration of Competing Interest

The authors declare that they have no known competing financial interests or personal relationships that could have appeared to influence the work reported in this paper.

Acknowledgements

The authors acknowledged Tertiary Education Trust Fund, Nigeria, with grant number (TETFUND/FUTMINNA/2017/10) for the sponsorship. The authors appreciate the contribution of the following people for their technical assistance: Dr Remy Bucher (XRD analysis, iThemba Labs, South Africa) and Dr Franscious Cummings (HRSEM/HRTEM/SAED/EDS) analysis, Physics department, University of the Western Cape (UWC), South Africa.

Supplementary materials

Supplementary material associated with this article can be found, in the online version, at doi:10.1016/j.clce.2022.100034.

References

Agarwal, S., Tyagi, I., Gupta, V.K., Golbaz, F., Golikand, A.N., Moradi, O., 2016. Synthesis and characteristics of polyaniline/zirconium oxide conductive nanocomposite for dye adsorption application. J. Mol. Liq. 218, 494–498.

Aghabeygi, S., Khademi-Shamami, M., 2018. ZnO/ZrO_2 nanocomposite: sonosynthesis, characterization and its application for wastewater treatment. UltrasonicsSonochemistry 41, 458–465.

Agorku, E.S., Kuvarega, A.T., Mamba, B.B., Pandey, A.C., Mishra, A.K., 2015. Enhanced visible-light photocatalytic activity of multi-elements-doped ZrO_2 for degradation of indigo carmine. J. Rare Earths 33 (5), 498–506.

Ahmad, I., Alamgir, K., Gul, I.H., 2020. Structural, magnetic and dielectric characteristics of optically tuned Fe doped ZrO, nanoparticles with visible light driven photocatalytic activity. Mater. Chem. Phys. 251, 122999.

Ahmed, T., Ren, H., Noman, M., Shahid, M., Liu, M., Ali, M.A., Li, B., 2021. Green synthesis and characterization of zirconium oxide nanoparticles by using a native Enterobacter sp. and its antifungal activity against bayberry twig blight disease pathogen Pestalotiopsis versicolor. Nano Impact 21, 100281.

Al-Zaqri, N., Muthuvel, A., Jothibas, M., Alsalme, A., Alharthi, F.A, Mohana, V., 2021. Biosynthesis of zirconium oxide nanoparticles using *Wrightia tinctoria* leaf extract: characterization, photocatalytic degradation and antibacterial activities. Inorg. Chem. Commun. 127, 108507.

Alagarsamy, A., Chandrasekaran, S., Manikandan, A., 2022. Green synthesis and characterization studies of biogenic zirconium oxide (ZrO_2) nanoparticles for adsorptive removal of methylene blue dye. J. Mol. Struct. 1247, 131275.

Ameta, R., Solanki, M.S., Benjamin, S., &Ameta, S.C., 2018. Photocatalysis. Adv. Oxid. Process. Waste Water Treat. 3 (3), 135–175.

Anandan, K., Rajesh, K., Gayathri, K., Sharma, S.V., Hussain, S.M., &Rajendran, V., 2020. Effects of rare earth, transition and post transition metal ions on structural and optical properties and photocatalytic activities of zirconia (ZrO_2) nanoparticles synthesized via the facile precipitation process. Phys. E 124, 114342.

Aneyo, I.A., Doherty, F.V., Adebesin, O.A., Hammed, M.O., 2016. Biodegradation of pollutants in waste water from pharmaceutical, textile and local dye effluent in Lagos, Nigeria. J. Health Pollut. 6 (12), 34–42.

Anku, W.W., Oppong, S.O.B., Shukla, S.K., Agorku, E.S., Govender, P.P., 2016. Cobalt doped ZrO_2 decorated multiwalled carbon nanotube: a promisingnanocatalyst for photodegradation of indigo carmine and eosin Y dyes. Prog. Natl Sci. Mater. Int. 26 (4), 354–361.

Arjun, A., Dharr, A., Raguram, T., Rajni, K.S., 2020. Study of copper doped zirconium dioxide nanoparticles synthesized via sol–gel technique for photocatalytic applications. J. Inorg. Organomet. Polym. Mater. 30, 4989–4998.

Bailón-García, E., Elmouwahidi, A., Carrasco-Marín, F., Pérez-Cadenas, A.F., &Maldonado-Hódar, F.J., 2017. Development of carbon-ZrO_2 composites with high performance as visible-light photocatalysts. Appl. Catal. B 217, 540–550.

Bhalodia, N.R., Shukla, V.J., 2011. Antibacterial and antifungal activities from leafextracts of cassia fistula l.: an Ethno-medicinal plant. J. Adv. Pharm. Technol. Res. 2, 104–109.

Bharathi, E., Sivakumari, G., Karthikeyan, B., Senthilvelan, S., 2020. Hydrothermal implement with supporting of semiconductor ZrO_2 (ZO), Ag doped ZrO_2 (AZO) nanomaterial and its astrophysical, UV photocatalytic employment on Rh6G dye. Appl. Nanosci. 10, 3491–3502.

Bhowmik, M., Debnath, A., Saha, B., 2018. Fabrication of mixed phase calcium ferrite and zirconia nanocomposite for abatement of methyl orange dye from aqua matrix: optimization of process parameters. Appl. Organometal. Chem. 32 (12), e4607.

Bommalapura Hanumaiah, A., Al-Gunaid, M.Q., 2021. Performance of nano-K-doped zirconate on modified opto-electrical and electrochemical properties of gelatin biopolymer nanocomposites. Polym. Bull. 78 (6), 3023–3041.

Buszewski, B., Rafińska, K., Cvetanović, A., Walczak, J., Krakowska, A., Rudnicka, J., &Zeković, Z., 2019. Phytochemical analysis and biological activity of Lupinus luteusseeds extracts obtained by supercritical fluid extraction. Phytochem. Lett. 30, 338–348.

Danilenko, I., Gorban, O., Gorban, S., Volkova, G., Glazunova, V., &Konstantinova, T., 2018. Production of composite ZrO_2-ZnO nanoparticles using advanced Co-precipitation process and determination their photo-oxidative properties by oxidation of C60 fullerene. In: Proceedings of the *IEEE 8th International Conference Nanomaterials: Application & Properties (NAP)* (1-5).

Daoud, A., Malika, D., Bakari, S., Hfaiedh, N., Mnafgui, K., Kadri, A., et al., 2015. Assessment of polyphenol composition, antioxidant and antimicrobial properties ofvarious extracts of date palm pollen (DPP) from two Tunisian cultivars. Arab. J. Chem. doi:10.1016/j.arabjc.2015.07.014, (in press).

Dawoud, T.M.S., Pavitra, V., Ahmad, P., Syed, A., Nagaraju, G., 2020. Photocatalytic degradation of an organic dye using Ag doped ZrO_2 nanoparticles: milk powder facilitated eco-friendly synthesis. J. King Saud Univ. Sci. 32, 1872–1878.

Davoodbeygi, Y., Irankhah, A., 2018. Nanostructured CeCu mixed oxide synthesized by solid state reaction for medium temperature shift reaction: optimization using response surface method. Int. J. Hydrog. Energy 43 (49), 22281–22290.

Debnath, B., Majumdar, M., Bhowmik, M., Bhowmik, K.L., Debnath, A., Roy, D.N., 2020. The effective adsorption of tetracycline onto zirconia nanoparticles synthesized by novel microbial green technology. J. Environ. Manag. 261, 110235.

Dharr, A., Arjun, A., Raguram, T., Rajni, K.S., 2020. Influence of pH on the structural, spectral, optical, morphological and photocatalytic properties of ZrO_2 nanoparticles synthesized by sol–gel technique. J. Mater. Sci. Mater. Electron. 31 (18), 15718–15730.

Długosz, O., Szostak, K., Banach, M., 2019. Photocatalytic properties of zirconium oxide–zinc oxide nanoparticles synthesised using microwave irradiation. Appl. Nanosci. 10, 941–954.

Egbosiuba, T.C., Abdulkareem, A.S., 2021. Highly efficient as-synthesized and oxidized multi-walled carbon nanotubes for copper(II) and zinc(II) ion adsorption in a batch and fixed-bed process. J. Mater. Res. Technol. 15, 2848–2872.

Fakhri, A., Behrouz, S., Tyagi, I., Agarwal, S., Gupta, V.K., 2015. Synthesis and characterization of ZrO_2 and carbon-doped ZrO_2 nanoparticles for photocatalytic application. J. Mol. Liq. 216, 342–346.

Gião, M.S., González-Sanjosé, M.L., Rivero-Pérez, M.D., Pereira, C.I., Pintado, M.E., &Malcata, F.X., 2007. Infusions of portuguese medicinal plants: dependence of finalantioxidant capacity and phenol content on extraction features. J. Sci. Food Agric. 87 (14), 2638–2647.

Gordon, M.H., Paiva-Martins, F., Almeida, M., 2001. Antioxidant activity ofhydroxytyrosol acetate compared with that of other olive oil polyphenols. J. Agric. Food Chem. 49 (5), 2480–2485.

Guo, Z., Ma, T., Xu, T., Chen, Y., Yang, G., Li, Y., 2020. Amorphous Li_2ZrO_3 nanoparticles coating Li [Li0· 17Mn0· 58Ni0. 25] O_2 cathode material for enhanced rate and cyclic performance in lithium ion storage. Mater. Chem. Phys. 255, 123593.

Haq, S., Afsar, H., Ali, M.B, Almalki, M., Albogami, B., Hedfi, A., 2021. Green synthesis and characterization of a ZnO-ZrO_2 heterojunction for environmental and biological applications. Crystals 11, 1502 2021.

Hardin, A., Crandall, P.G., Stankus, T., 2009. Essential oils and antioxidants derived fromcitrus by-products in food protection and medicine: an introduction and review of recentliterature. J. Agric. Food Inf. 11 (2), 99–122.

Irawan, C., Putra, M.D., Nata, I.F., Refki, M.F., Hidayat, R., Abbas, A.T., 2022. Synthesis of composite nanostructure natural ZrO_2 and magnetite particles (Fe_3O_4@ZrO_2) and study of its lead ion adsorption efficiency. IOP Conf. Ser. Mater. Sci. Eng. 1212, 012016.

Kadi, M.W., Mohamed, R.M., 2013. Enhanced photocatalytic activity of ZrO_2-SiO_2 nanoparticles by platinum doping. Int. J. Photoenergy 2013, 7 Article ID 812097pages.

Kalampaliki, T., Makri, S.P., Papadaki, E., Grigoropoulos, A., Zoikis Karathanasis, A., Deligkiozi, I., 2021. Visible-light active sulfur-doped Titania nanoparticles immobilized on a silica matrix: synthesis, characterization and photocatalytic degradation of pollutants. Nanomaterials 11, 2543.

Kaliraj, L., Ahn, J.C., Rupa, E.J., Abid, S., Lu, J., Yang, D.C., 2019. Synthesis of panosextract mediated ZnO nano-flowers as photocatalyst for industrial dye degradation by UV illumination. J. Photochem. Photobiol. B 199, 111588.

Kaviya, S., 2020. Evolution of ZnO-based photocatalyst for the degradation of pollutants. Green Photocatalysts for Energy and Environmental Process, Springer, 109-139.
Keshavarz-Shokri, A., Zhang, B., Alcacio, T.E., Lee, E.C., Zhang, Y., Krawiec, M., 2018. U.S. PatentNo. 10,081,621. U.S. Patent and TrademarkOffice, Washington, DC.
Kianfar, A.H., Arayesh, M.A., &Momeni, M.M., 2021. Degradation of MB and RhB by modified ZrO_2 nanoparticles via sunlight. Appl. Phys. A 127 (2), 1–9.
Kurakaran, S., George, A., Nair, A.S., 2014. Synthesis and characterization of zirconium oxide nanoparticle prepared by aqueous gelation method. J. Indian Chem. Soc. 91 (1), 47–52.
Majedi, A., Abbasi, A., Davar, F., 2015. Green synthesis of zirconia nanoparticles using the modified Pechini method and characterization of its optical and electrical properties. J. Sol Gel Sci. Technol. doi:10.1007/s10971-015-3881-3.
Malyi, O.I., Chen, Z., Shu, G.G., Wu, P., 2011. Effect of sulfur impurity on the stability of cubic zirconia and its interfaces with metals. J. Mater. Chem. 21 (33), 12363–12368.
Melchor-Lagar, V., Ramos-Ramírez, E., Morales-Pérez, A.A., Rangel-Vázquez, I., Del Angel, G., 2020. Photocatalytic removal of 4-chlorophenol present in water using ZrO_2/LDH under UV light source. J. Photochem. Photobiol. A 389, 112251.
Mondal, S., Reyes, M.E.D.A., Pal, U., 2017. Plasmon induced enhanced photocatalytic activity of gold loaded hydroxyapatite nanoparticles for methylene blue degradation under visible light. RSC Adv. 7 (14), 8633–8645.
Nigerian Industrial Standard (NIS), 2007. Nigerian Standard for Drinking Water Quality. NIS554. Stand. Organ. Niger. 2007, 1–30. Nigerian Industrial Standard (NIS), 2007. Nigerian Standard for Drinking Water Quality. NIS554. Stand. Organ. Niger. 2007, 1–30.
Nova, C.V., Reis, K.A., Pinheiro, A.L., Dalmaschio, C.J., Chiquito, A.J., Teodoro, M.D., Rodrigues, A.D., Longo, E., Pontes, F.M., 2021. Synthesis, characterization, photocatalytic, and antimicrobial activity of ZrO_2 nanoparticles and Ag@ZrO_2 nanocomposite prepared by the advanced oxidative process/hydrothermal route. J. Sol Gel Sci. Technol. 98, 113–126.
Park, S., Shao, G., 2019. Microstructure and materials characterization of sol-gel synthesized ZrO_2 systems. Tanzan. J. Sci. 45 (2), 190–208.
Rajesh, G., Akilandeswari, S., Govindarajan, D., Thirumalai, K., 2020. Enhancement of photocatalytic activity of ZrO_2 nanoparticles by doping with Mg for UV light photocatalytic degradation of methyl violet and methyl blue dyes. J. Mater. Sci. Mater. Electron. 31 (5), 4058–4072.
Rani, S., Aggarwal, M., Kumar, M., Sharma, S., Kumar, D., 2016. Removal of methylene blue and rhodamine B from water by zirconium oxide/graphene. Water Sci. 30 (1), 51–60.
Reddy, C.V., Reddy, I.N., Ravindranadh, K., Reddy, K.R., Kim, D., Shim, J., 2020. Ni–dopant concentration effect of ZrO_2 photocatalyst on photoelectrochemical water splitting and efficient removal of toxic organic pollutants. Sep. Purif. Technol. 252, 117352.
Renuka, L., Anantharaju, K.S., Gurushantha, K., Nagabhushana, H., Vidya, Y.S., Suresh, C., Sennappan, M., 2021. Phase-transformation synthesis of Li codoped ZrO_2Eu^{3+} nanomaterials: characterization, photocatalytic, luminescent behaviour and latent fingerprint development. Ceram. Int. 47 (7), 10332–10345.
Rivero-Cruz, J.F., Granados-Pineda, J., Pedraza-Chaverri, J., Pérez-Rojas, J.M., KumarPassari, A., Diaz-Ruiz, G., Rivero-Cruz, B.E., 2020. Phytochemical constituents,antioxidant, cytotoxic,and antimicrobial activities of the ethanolic extract of mexicanbrownpropolis. Antioxidants 9 (1), 70.
Saraswathi, V.S., Santhakumar, K., 2017. Photocatalytic activity against azo dye and cytotoxicity on MCF-7 cell lines of zirconium oxide nanoparticle mediated using leaves of Lagerstroemia speciosa. J. Photochem. Photobiol. B 169, 47–55.
Shinde, H.M., Bhosale, T.T., Gavade, N.L., Babar, S.B., Kamble, R.J., Shirke, B.S., &Garadkar, K.M., 2018. Biosynthesis of ZrO_2 nanoparticles from Ficusbenghalensisleaf extract for photocatalytic activity. J. Mater. Sci. Mater. Electron. 29 (16), 14055–14064.
Singh, A.K, Nakate, U.T., 2014. Microwave synthesis, characterization, and photoluminescence properties of nanocrystalline zirconia. Sci. World J. 2014, 7 Article ID 349457pages.
Song, C., Chen, K., Chen, M., Jin, X., Liu, G., Du, X., Chen, D., Huang, Q., 2022. Sequential combined adsorption and solid-phase photocatalysis to remove aqueous organic pollutants by H_3PO_4 -modified TiO_2 nanoparticles anchored on biochar. J. Water Process Eng. 45, 102467.
Sun, J., Kormakov, S., Liu, Y., Huang, Y., Wu, D., Yang, Z., 2018. Recent progress in metal-based nanoparticles mediated photodynamic therapy. Molecules 23 (7), 1704.
Su, Y., Cui, H., Li, Q., Gao, S., Shang, J.K., 2013. Strong adsorption of phosphate by amorphous zirconium oxide nanoparticles. Water Res. 47, 5018–5026.
Szatmáry, L., Bakardjieva, S., Šubrt, J., Bezdička, P., Jirkovský, J., Bastl, Z., Korenko, M., 2011. Sulphur doped nanoparticles of TiO_2. Catal. Today 161 (1), 23–28.
Tsegaye, F., Taddesse, A.M., Teju, E., Aschalew, M., 2020. Preparation and sorption property study of $Fe_3O_4/Al_2O_3/ZrO_2$ composite for the removal of cadmium, lead and chromium ions from aqueous solutions. Bull. Chem. Soc. Ethiop. 34 (1), 105–121.
Uribe López, M.C., Lemus, M.A., Hidalgo, M.C., López, R., Quintana, P., Oros, S., Acosta, J., 2019. Structural and optical characterization of ZnO-ZrO_2 nanocomposites for photocatalytic degradation and mineralization of phenol. J. Nanomater. 2019, 35–64 Article ID 1015876, 12 pages123.
Wahba, M.A., Yakout, S.M., Mohamed, W.A., Galal, H.R., 2020. Remarkable photocatalytic activity of Zr doped ZnO and ZrO_2/ZnO nanocomposites: structural, morphological and photoluminescence properties. Mater. Chem. Phys. 256, 123754.
Wang, Z., Fang, W., Xing, M., Wu, D., 2017. A bench-scale study on the removal and recovery of phosphate by hydrous zirconia-coated magnetite nanoparticles. J. Magn. Magn. Mater. 424, 213–220.
Wang, Y., Zhang, Y., Lu, H., Chen, Y., Liu, Z., Su, S., Xue, Y., Yao, J., Zeng, H., 2018. Novel N-doped ZrO_2 with enhanced visible-light photocatalytic activity for hydrogen production and degradation of organic dyes. R. Soc. Chem. Adv. 8, 6752.
Wei, G., Qi, J., Lin, P., Pan, S., Sun, X., Shen, J., Han, W., Wang, L., Li, J., 2018. Polyethersulfone enwrapped hydrous zirconium oxide nanoparticles for efficient removal of Pb(II) from aqueous solution. Chem. Eng. J. 349, 500–508.
World Health Organization, 2017. Safely Managed Drinking Water: Thematic Report on Drinking Water 2017.
Xu, H., Shen, X., Khan, M.A., Wang, F., Lei, W., Xia, M., 2020. Facile synthesis of rock-like Ag_2ZrO_3 decorated with TiO_2 nanoparticles heterostructures with highly enhanced visible-light photocatalytic properties. J. Nanopart. Res. 22 (3), 1–13.
Yadav, P., Dwivedi, P.K., Tonda, S., Boukherroub, R., &Shelke, M.V., 2020. Metal and non-metal doped metal oxides and sulfides. Green Photocatalysts, Book Chapter Published by Springer 34, 89–132.
Yousefi, R., Beheshtian, J., Seyed-Talebi, S.M., Azimi, H.R., Jamali-Sheini, F., 2018. Experimental and theoretical study of enhanced photocatalytic activity of Mg-doped ZnO NPs and ZnO/rGO nanocomposites. Chem. An Asian J. 13 (2), 194–203.
Zhang, C., Li, Y., Wang, F., Yu, Z., Wei, J., Yang, Z., Ma, C., Li, Z., Xu, Z., Zeng, G., 2017. Performance of magnetic zirconium-iron oxide nanoparticle in the removal of phosphate from aqueous solution. Appl. Surf. Sci. 396, 1783–1792.
Zarei, M., Bahrami, J., Zarei, M., 2019. Zirconia nanoparticle-modified graphitic carbon nitride nanosheets for effective photocatalytic degradation of 4-nitrophenol in water. Appl. Water Sci. 9 (8), 1–11.
Zhang, X., Li, L., Zhou, Q., Liang, X., Liu, D., 2019. Facile synthesis of novel gully-like double-sized mesoporous structural Sr-doped ZrO_2–TiO_2 composites with improved photocatalytic efficiency. J. Solid State Chem. 269, 375–385.
Zhang, K., Zhou, M., Yu, C., Yang, K., Li, X., Dai, W., Huang, W., 2020. Construction of S-scheme g-C_3N_4/ZrO_2 heterostructures for enhancing photocatalytic disposals of pollutants and electrocatalytic hydrogen evolution. Dyes Pigment. 180, 108525.